Icarus 452 (2026) 117049

Contents lists available at ScienceDirect

Icarus

journal homepage: www.elsevier.com/locate/icarus

Research paper

A re-assessment of moderately volatile elements in the non-matrix component of carbonaceous chondrites

Zhongtian Zhang [a],*, Damanveer S. Grewal [b]

[a] Department of Geosciences, Princeton University, Princeton, NJ, USA
[b] Department of Earth and Planetary Sciences, Yale University, New Haven, CT, USA

ARTICLE INFO

Keywords:
Carbonaceous chondrites
Moderately volatile elements
Chondrule
Matrix
Two-component mixing
Isotopic fractionation

ABSTRACT

All carbonaceous chondrites are variably depleted in moderately volatile elements (MVEs) relative to CI chondrites, which closely match the bulk composition of the Solar System. This MVE depletion is thought to reflect mixing between a CI-like matrix and an MVE-depleted non-matrix component. Since the non-matrix component is primarily composed of chondrules, constraining the extent of MVE depletion in the non-matrix component is critical for understanding chondrule formation. Two approaches have been applied previously to estimate MVE abundances in the non-matrix component, yielding differing predictions. The first relies solely on chondrite compositions, while the second combines chondrite compositions with matrix mass fractions. The latter, which has gained wide acceptance, predicts that the abundances of MVEs with 50% nebular condensation temperatures below ~750 K (the so-called "plateau" MVEs) in the non-matrix component are ~0.13×CI. These estimated abundances have been further used to constrain the mass-dependent isotopic compositions of MVEs in the non-matrix (or chondrule) component. However, the matrix mass fractions employed in these fits have been challenged by detailed analyses of several carbonaceous chondrite groups. In this study, we use the revised matrix mass fractions to re-assess the MVE contents of the non-matrix component in carbonaceous chondrites. The results suggest that many MVEs occur in the non-matrix component at levels below ~0.13×CI abundances, consistent with the first approach that does not use matrix mass fractions as input data. Based on our new results, the mass-dependent isotopic fractionations for "plateau" MVEs such as Zn and Te between matrix and non-matrix components are inferred to be larger than previously estimated. We discuss the possible origins of the elemental and isotopic compositions of the non-matrix component and suggest that they can be explained by chondrule formation alone, without invoking inheritance from chondrule precursors.

1. Introduction

Moderately volatile elements (MVEs) are elements with 50% nebular condensation temperatures below Mg silicates and Fe-Ni metal but above those of highly volatile elements such as H, C, N, and noble gases (e.g., Palme et al., 2014). Although some studies define MVEs as elements with 50% condensation temperatures higher than ~650 K, we adopt the broader definition to include more volatile elements such as Zn and Te. MVE depletion patterns in primitive meteorites provide key constraints on early Solar System processes. Carbonaceous chondrites, which are undifferentiated meteorites representing the bulk compositions of outer Solar System planetesimals, exhibit systematic variations in MVE abundances among different groups. CI chondrites closely match the bulk Solar System composition, whereas all other carbonaceous chondrite groups exhibit variable MVE depletions relative to CI (e.g., Davis, 2006; Palme et al., 2014). This variation has been attributed to two-component mixing of low-temperature, volatile-rich CI-like matrix and high-temperature, volatile-depleted non-matrix materials (e.g., Anders, 1964; Larimer and Anders, 1967; Alexander, 2005, 2019; Braukmüller et al., 2018, 2025; Hellmann et al., 2020). This two-component mixing model has been particularly successful in quantitatively reproducing both MVE abundances and isotopic variations across carbonaceous chondrite groups (e.g., Alexander, 2019; Hellmann et al., 2020, 2023; Nie et al., 2021; Morton et al., 2024; Wölfer et al., 2025).

The non-matrix fraction of carbonaceous chondrites comprises chondrules and refractory inclusions. Because refractory inclusions account for only a small fraction of the non-matrix component and are almost MVE-free, the MVE budget of the non-matrix component is dominated by chondrules. Accurately constraining MVE abundances and isotopic compositions in the non-matrix component provides critical constraints on chondrule formation (e.g., Hellmann et al., 2020; Nie et al., 2021;

* Corresponding author.
E-mail address: zhongtian.zhang@princeton.edu (Z. Zhang).

https://doi.org/10.1016/j.icarus.2026.117049
Received 29 January 2026; Received in revised form 3 March 2026; Accepted 12 March 2026
Available online 13 March 2026

Braukmüller et al., 2025; Jacquet et al., 2026), a long-standing problem in planetary science (e.g., Alexander and Ebel, 2012; Desch et al., 2012; Connolly and Jones, 2016; Marrocchi et al., 2024; Stewart et al., 2025).

All components of carbonaceous chondrites have been modified by aqueous alteration and/or thermal metamorphism in their parent bodies (e.g., Grossman and Brearley, 2005; Brearley and Krot, 2013; Alexander, 2019; van Kooten et al., 2024). Therefore, their primitive MVE abundances and isotopic compositions may not be easily obtained by direct measurements. Instead, these values can be inferred indirectly from comparing bulk compositions of different chondrite groups. Two different approaches have been used for this purpose. Alexander (2019) fitted the bulk compositions of carbonaceous chondrite groups and inferred the compositions of their constituent components by minimizing the misfit in bulk data, treating the component mass fractions as fitting parameters rather than inputs. In contrast, Hellmann et al. (2020) combined the bulk chondrite MVE abundances with estimated matrix mass fractions to derive correlations between MVE concentrations and matrix mass fractions, which were then extrapolated to zero matrix mass fraction to infer MVE abundances in the non-matrix component. The two studies yielded different estimates for several MVEs. For instance, Hellmann et al. (2020) suggested that the non-matrix component contains a Zn abundance of ~0.13×CI (as part of a "plateau" representing nearly constant CI-normalized abundances for MVEs with 50% condensation temperatures lower than ~750 K), whereas Alexander (2019) suggested that the Zn concentration of the non-matrix component is nearly zero.

These differences are important for constraining the physicochemical conditions of chondrule formation. Hellmann et al. (2020) interpreted the presence of a "plateau" in the non-matrix component as evidence against elemental and isotopic fractionation during chondrule formation. However, if the lower abundances proposed by Alexander (2019) are adopted, this argument would not hold. The differing estimates also have major implications for the isotopic compositions of the "plateau" MVEs in the non-matrix (or chondrule) component. There is an intrinsic trade-off between the estimated abundance and isotopic composition of an MVE in the non-matrix component. To reproduce the observed offset of bulk carbonaceous chondrites from the CI-like matrix isotopic composition, an MVE in the non-matrix component can be assigned either a relatively high abundance with a modest isotopic fractionation, or a low abundance with a correspondingly large isotopic fractionation. For instance, assuming the non-matrix abundance proposed by Hellmann et al. (2023), the non-matrix $\delta^{66/64}$Zn has been estimated to be ~0.4–0.6‰ lower than CI chondrites (Nie et al., 2021; Morton et al., 2024). However, the same data can also be explained by a non-matrix abundance as low as ~0.005×CI if the fractionation between the non-matrix and matrix components is as large as the theoretical limit of pure kinetic condensation (Braukmüller et al., 2025). As isotopic fractionation during volatile loss and recondensation is sensitive to the physicochemical conditions of the chondrule-forming environment (e.g., Nie et al., 2021; Jacquet et al., 2026), accurately determining the non-matrix MVE abundances is critical for understanding chondrule formation.

Given that the approach of Hellmann et al. (2020) has been widely adopted in subsequent studies (e,g., Hellmann et al., 2023; Nie et al., 2021; Morton et al., 2024; Wölfer et al., 2025), it is critical to evaluate the validity of their input data. Among the model parameters, the matrix mass fractions of the carbonaceous chondrite groups carry the largest uncertainty. Hellmann et al. (2020) estimated these fractions from measured volume fractions and assumed component densities. Recently, Patzer et al. (2021, 2022, 2023) determined the mass fractions of different components in CM, CO, and CR chondrites more rigorously, obtaining matrix mass fractions of ~54%, ~30%, and ~22%, which are notably higher than those (~41%, ~20%, and ~9%) estimated by Hellmann et al. (2020) (see Appendix A for details). It remains unclear (i) how the MVE estimates would be affected if these revised matrix mass fractions are used, (ii) how the updated results would compare with those of Alexander (2019), and (iii) what implications these updates would have for the isotopic compositions of chondrules. In this study, we re-assess the MVE contents of the non-matrix component of carbonaceous chondrites, quantify their associated uncertainties, and discuss the implications of this re-assessment.

2. Methods

2.1. MVE concentrations and matrix fractions of carbonaceous chondrite groups

We follow the approach of Hellmann et al. (2020), examining the relationships between MVE concentrations and carbonaceous chondrite matrix mass fractions. Hellmann et al. (2020) estimated matrix mass fractions based on measured volume fractions of individual components, measured densities of bulk chondrites, and assumed densities for each component. This method provides reasonable first-order estimates, and the resulting values have been widely used in recent studies on MVEs in carbonaceous chondrites (e.g., Hellmann et al., 2023; Nie et al., 2021; Morton et al., 2024; Wölfer et al., 2025). However, both the component volume fractions and densities involve considerable uncertainties, and the accuracy of some of their estimates have been challenged by more detailed analyses (Patzer et al., 2021, 2022, 2023).

Hellmann et al. (2020) considered six groups of carbonaceous chondrites: CI, CM, CV, CO, CR, and C2-ungrouped Tagish Lake. For the CM, CO, and CR, updated matrix mass fractions provided by Patzer et al. (2021, 2022, 2023) are 54.2 ± 10.1% (CM), 31.1 ± 11.0% (CO), and 17.1 ± 7.1% (CR, with Renazzo being excluded; see Appendix A). These values are substantially different from those reported by Hellmann et al. (2020), 40.9 ± 11.8% (CM), 22.9 ± 11.6% (CO), and 8.9 ± 5.1% (CR) (uncertainties represent two standard deviations). For these three groups, we adopt the updated values of Patzer et al. (2021, 2022, 2023) (also Appendix A for detailed discussion). For CI chondrites, which are generally considered to be entirely matrix, the matrix mass fraction is assumed to be 100% as in Hellmann et al. (2020). For CV chondrites, no detailed study equivalent to that of Patzer et al. (2021, 2022, 2023) exists. Nevertheless, CV chondrites exhibit broadly similar matrix volume fractions and MVE abundances to CO chondrites (Alexander, 2019; Hellmann et al., 2020). Since MVE contents correlate positively with the matrix mass fractions, and CV-CO differences in MVE concentrations are typically within analytical uncertainties (Fig. 1), we consider the CV matrix mass fraction to be comparable to that of CO chondrites. As the Hellmann et al. (2020) estimate for CV chondrites (30.5 ± 7.3%) closely matches the updated CO value (31.1 ± 11.0%), we retain the CV group estimate from Hellmann et al. (2020) (also see Appendix A for more discussion). The case for Tagish Lake is more problematic. The value used by Hellmann et al. (2020) was estimated without any density correction (i.e., the matrix volume fraction was directly used as mass fraction). Moreover, the matrix volume fraction was calculated as the average of only a few samples that exhibit large variations (Blinova et al., 2014), calling into question the representativeness of the volume fraction value itself. Given the lack of more detailed analyses for Tagish Lake samples, it is difficult to assign them a reliable matrix mass fraction. Thus, we exclude it from our fitting. The matrix mass fractions adopted in this study and their uncertainties are summarized in Table 1.

We consider the concentrations of a wide suite of MVEs, including Na, S, K, Mn, Cu, Zn, Ga, Ge, As, Se, Rb, Ag, Cd, In, Sn, Te, Cs, and Tl. To ensure consistency in data sources for different elements, we take the concentrations of all MVEs (except Ge) from Braukmüller et al. (2018, 2019, 2025). Some apparently anomalous data, such as the Na concentrations of several CM chondrite samples, are excluded (see Appendix B). For Ge, which was not measured by Braukmüller et al. (2018, 2019, 2025), the concentrations are taken from Wölfer

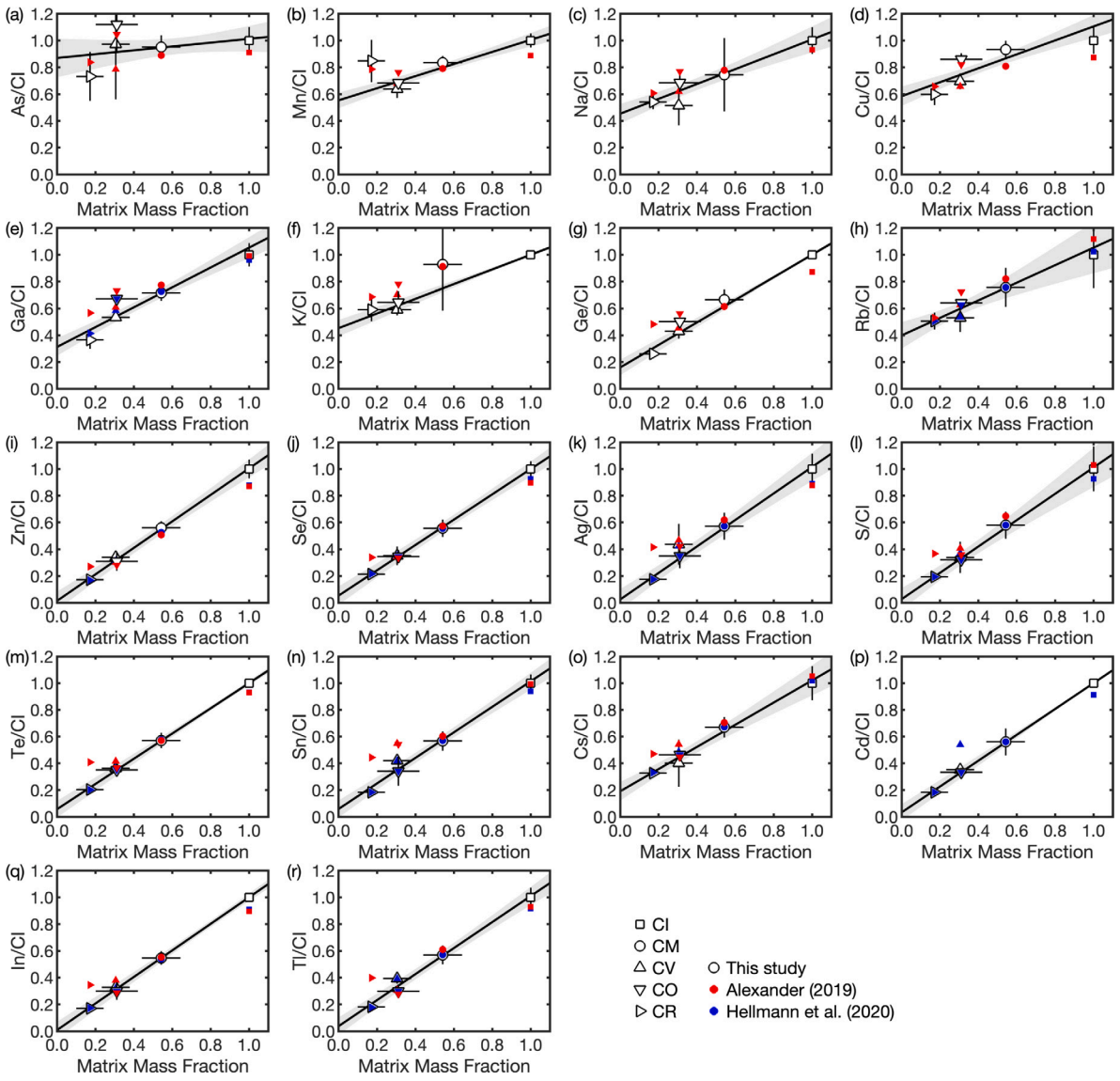

Fig. 1. MVE abundances in carbonaceous chondrite groups versus updated matrix mass fractions. The white circles are concentrations used in this study, the red and blue symbols are the concentrations used in Alexander (2019) and Hellmann et al. (2020), respectively. The black lines and the gray regions are the best-fit results and the error envelopes of the fitting. The values shown on the y-axes are normalized by the mean CI chondrite concentrations given in Table 2 (after the sulfate oxygen correction). The CI chondrite concentrations used in Alexander (2019) and Hellmann et al. (2020) do not plot at one on the *y*-axis because they are not identical to the CI concentrations used here for the normalization.

et al. (2025). For CI chondrites, we make an additional revision to account for the effect of secondary sulfates. Most CI chondrite samples analyzed by previous studies contain abundant sulfates, with sulfate oxygen contributing ~7.35% of the total mass (Alexander, 2019). These sulfates are now recognized as products of terrestrial oxidation of sulfides due to the absence of sulfates in samples returned from asteroids Ryugu and Bennu (which are chemically and isotopically similar to CI chondrites) as well as the fresh CI chondrite find, Oued Chebeika 002 (e.g., Yokoyama et al., 2023; Lauretta et al., 2024; Gattacceca et al., 2025). Hence, the sulfate oxygen in CI chondrites is presumably terrestrial, and the true concentrations of other elements in them should be $100/(100-7.35) \approx 1.08$ times the previously reported values. We correct all MVE concentrations in CI chondrites by a factor of 1.08. This correction is consistent with the observation that the concentrations of most elements in Ryugu samples are higher than those in CI chondrites by a factor of $\gtrsim$1.1 (Yokoyama et al., 2023).

2.2. MVE concentrations and isotopic compositions of the non-matrix component

We fit the data with a two-component mixing model,

$$c = kf + b, \tag{1}$$

where c is the concentration of an element in a given chondrite, f is the matrix mass fraction, and k and b are the slope and y-axis intercept of the linear relation, which can be expressed in terms of the concentrations in the matrix and non-matrix components, c_{M} and c_{NM}, as

$$k = c_{\mathrm{M}} - c_{\mathrm{NM}}, \quad b = c_{\mathrm{NM}}. \tag{2}$$

To account for uncertainties in both c and f, we apply the York method (York et al., 2004), which is described in detail in Appendix C, assuming that the errors in the two variables are uncorrelated. The fitting yields estimates and uncertainties of the parameters, which can be used to construct their posterior probability distributions conditional

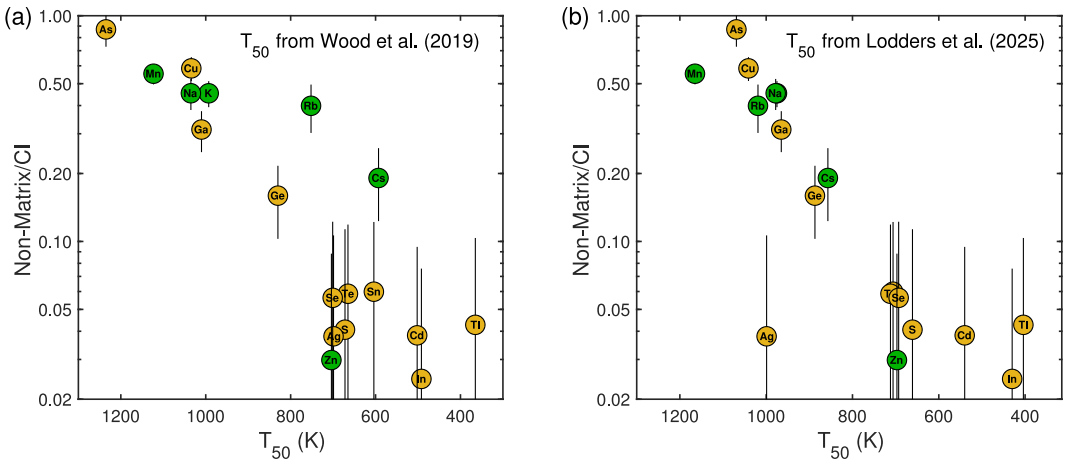

Fig. 2. The MVE concentrations of the non-matrix (chondrule) component versus the 50% condensation temperatures at total nebular pressure 10^{-4} bar from Wood et al. (2019) (a) and Lodders et al. (2025) (b). The green and yellow symbols indicate lithophile and siderophile/chalcophile elements. The vertical bars give the uncertainties of the non-matrix (chondrule) concentrations obtained from the fitting. The concentrations are normalized by the CI chondrite concentrations given in Table 2.

on the data. In the standard fitting, no prior constraints are imposed and the posterior distributions are normal (Gaussian); for each parameter, the mode, median, and mean of the posterior are identical and define the same "best estimate". Here, we are interested in the intercept b, which represents the non-matrix concentration of the considered MVE and thus must be positive. With this prior constraint, the negative part of the posterior distribution must be truncated. If the estimated value is comparable to or smaller than its uncertainty, the resulting distribution becomes asymmetric. In this case, the mode, mean, and median of the posterior are not identical, and the choice of the "best estimate" becomes somewhat ambiguous, although the differences among these values are within the fitting uncertainty.

We are also interested in the isotopic compositions of MVEs in the non-matrix component. The mixing of two components with distinct elemental and isotopic compositions leads to a linear relation between δ and $1/c$ of the mixture,

$$\delta = \alpha/c + \beta, \tag{3}$$

where δ is the isotopic composition of the bulk chondrite expressed in δ-notation. For a bulk carbonaceous chondrite, $\alpha = -c_{NM}c_M(\delta_{NM} - \delta_M)/(c_{NM} - c_M)$ and $\beta = (c_{NM}\delta_{NM} - c_M\delta_M)/(c_{NM} - c_M)$, where δ_M and δ_{NM} represent the isotopic compositions of the matrix and non-matrix components, respectively. Here, δ_{NM} is not known *a priori*, and α and β need to be obtained by fitting the δ and c data. In contrast to the c-f relation, which can only be fitted with data for average chondrite groups because reliable matrix mass fraction estimates for individual samples are scarce, the δ-$1/c$ relation can be fitted using data from individual samples because isotopic compositions are typically reported together with concentrations. When data from individual samples are used, no information is lost, and the parameters α and β can be better constrained. Hence, we fit the δ and $1/c$ data for individual samples. The data sources for isotopic compositions of MVEs are described in Appendix B. Again, we apply the York method (York et al., 2004). With α and β obtained from the δ-$1/c$ fitting, δ_{NM} can be calculated from c_{NM} following

$$\delta_{NM} = \alpha/c_{NM} + \beta. \tag{4}$$

The uncertainty in δ_{NM} arises from those of α, β, and c_{NM}. The last parameter can be particularly important, perhaps dominant, for elements like Zn and Te, for which (i) large numbers of measurements are available, making α and β well constrained, and (ii) c_{NM} is small, such that δ_{NM} is extremely sensitive to small changes in c_{NM} (see Section 3.3). Focusing on the contribution of c_{NM} uncertainty, we can transform the posterior distribution of c_{NM} to that of δ_{NM}. As this transformation is nonlinear, it shifts the position of the distribution mode. Consequently, the modes of the posterior distributions of c_{NM} and δ_{NM} do not form a pair that satisfies Eq. (4) (Fig. D.8), and choosing the modes as "best estimates" would lead to an inconsistency. In contrast, because the relation defined by Eq. (4) is monotonic, the median of c_{NM} naturally corresponds to the median of δ_{NM}, i.e., the medians of c_{NM} and δ_{NM} naturally form a consistent pair (Appendix D). For all elements, we choose the medians of the posterior distributions of c_{NM} as the best estimates and calculate the confidence intervals from the cumulative distributions. For δ_{NM}, we calculate the best estimates from the medians of c_{NM}, and evaluate the confidence intervals considering the uncertainties in c_{NM}, α, and β (see Appendix D for details).

Table 1
Matrix mass fractions of carbonaceous chondrite groups used in Hellmann et al. (2020) (H20) and this study.

	CI	CM	CV	CO	CR
H20	100%	40.9 ± 11.8%	30.5 ± 7.3%	20.2 ± 11.6%	8.9 ± 5.1%
This Study	100%	54.1 ± 10.1%	30.5 ± 7.3%	30.1 ± 11.0%	17.1 ± 7.1%

Notes: The uncertainties are given as two standard deviations. The matrix mass fractions of CM, CO, and CR chondrites are estimated from the values "corrected for mixed analyses" provided by Patzer et al. (2021, 2022, 2023). For CR chondrites, the results for Renazzo are excluded. For CV chondrites, we use the value from H20. See Section 2 and Appendix A for detailed discussion.

2.3. MVE versus Zn concentrations

In addition to the c-f relations, it is also helpful to examine the inter-correlations among the concentrations of different elements. This is because several limitations remain in obtaining precise data of group-averaged matrix mass fractions (and potentially elemental concentrations). One issue arises from intra-group variations in element concentrations and matrix mass fractions of carbonaceous chondrite samples. The matrix mass fraction and element concentration data should ideally be obtained from the same samples, but this is rarely possible. Moreover, the matrix mass fractions are obtained from a fundamentally different approach than the concentrations. Thus, combining the data for MVEs and matrix mass fractions may itself introduce a degree of self-inconsistency.

The problem of self-inconsistency can be addressed by examining the relationships between different elements. As the concentrations all correlate linearly with the matrix mass fraction, they should also correlate linearly with each other. By directly examining the correlations

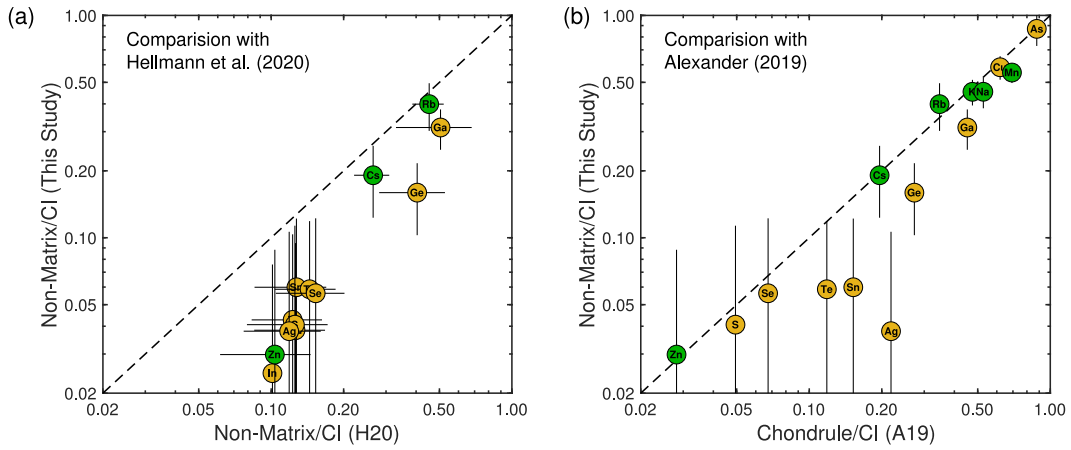

Fig. 3. Comparison of the non-matrix (chondrule) concentrations obtained in this study and those obtained by Hellmann et al. (2020) (a) and Alexander (2019) (b). All concentrations are normalized by the CI chondrite values given in Table 2. In Alexander (2019), the concentration of Zn in the "chondrule" component is assumed to be zero; to plot it here in log scale, we set it to be 10 μg/g, a value that can be considered small enough to be indistinguishable from zero in the Alexander (2019) model.

Table 2
MVE abundances of CI chondrites (after the sulfate oxygen correction) and the non-matrix (NM) component from Alexander (2019) (A19), Hellmann et al. (2020) (H20), and matrix-based and Zn-based fittings of this study. In the Zn-based fitting, the non-matrix concentration of Zn is taken as the "best estimate" from the matrix-based fitting.

	CI	NM (A19)	NM (H20)		NM (Matrix)		NM (Zn, "best")	
	b.e.	b.e.	b.e.	95% c.i.	b.e.	95% c.i.	b.e.	95% c.i.
Na (mg/g)	5.3	2.8			2.4	(2.0, 2.8)	1.8	(1.6, 2.1)
S (mg/g)	52	2.6	6.5	(4.1, 8.9)	2.1	(0.1, 5.9)	2.7	(1.4, 4.0)
K (μg/g)	442	210			200	(174, 226)	195	(176, 213)
Mn (mg/g)	2.2	1.5			1.2	(1.1, 1.3)	1.3	(1.2, 1.4)
Cu (μg/g)	152	94			89	(78, 100)	84	(78, 91)
Zn (μg/g)	355	0	37	(22, 52)	11	(1, 31)	11	–
Ga (μg/g)	9.7	4.4	4.9	(3.2, 6.6)	3.0	(2.4, 3.7)	2.7	(2.4, 3.0)
Ge (μg/g)	37	10	15	(10, 20)	6.0	(3.8, 8.1)	8.3	(6.1, 11)
As (μg/g)	1.9	1.7			1.7	(1.4, 1.9)	1.5	(1.4, 1.6)
Se (μg/g)	22	1.5	3.5	(2.4, 4.6)	1.3	(0.1, 2.8)	1.8	(1.2, 2.3)
Rb (μg/g)	2.1	0.72	0.94	(0.80, 1.08)	0.83	(0.63, 1.02)	0.80	(0.73, 0.88)
Ag (ng/g)	228	49	27	(17, 37)	8.7	(0.5, 24)	9.2	(4.0, 14)
Cd (μg/g)	0.75		0.10	(0.07, 0.13)	0.03	(0.00, 0.07)	0.03	(0.01, 0.05)
In (ng/g)	87		9	(6, 12)	2.0	(0.1, 6.3)	2.4	(0.5, 4.3)
Sn (μg/g)	1.6	0.25	0.21	(0.14, 0.28)	0.10	(0.01, 0.20)	0.09	(0.05, 0.12)
Te (μg/g)	2.5	0.29	0.35	(0.25, 0.45)	0.14	(0.02, 0.29)	0.16	(0.10, 0.21)
Cs (ng/g)	179	35	47	(39, 55)	34	(22, 46)	30	(25, 36)
Tl (ng/g)	151		19	(13, 25)	6.4	(0.5, 16)	6.0	(2.6, 9.4)

between different elements, we can avoid the matrix mass fraction data, which represent the main source of potential inconsistency. Also, by considering the inter-correlations of different elements, we can directly use the data from individual samples to maximize the use of available information. Furthermore, by plotting all data from individual samples, we can better examine the origins of intra-group variability, which can only be treated as error bars when the group averages are used, to examine whether they represent random errors or intrinsic factors such as varying matrix mass fractions.

Here, we choose Zn as the reference element (x-axis) for several reasons previously pointed out by Alexander (2019): First, its abundances in bulk chondrites are sufficiently high to allow precise and reproducible measurements. Second, Zn is not significantly affected by terrestrial contamination (unlike Pb) or parent body thermal metamorphism and shock processes (unlike Cd). Third, its abundance in the non-matrix component is much lower than that in the matrix, making it a sensitive tracer of the matrix mass fraction. For all measurements, the two-standard-deviation uncertainty is taken to be 10% of the concentrations.

Despite the advantages, this approach also has a key shortcoming: to calculate the non-matrix MVE concentrations, its Zn concentration must be assumed. We choose several values within the confidence interval provided by the matrix-based fitting. Thus, the estimates for the non-matrix component are still dependent on the matrix mass fraction data, but this practice allows us to evaluate the consistency of the results across different elements from the matrix-based fitting. It also provides an opportunity to assess the matrix mass fractions of CV and Tagish Lake, which are either assumed or excluded in the matrix-based fitting.

3. Results

3.1. MVE concentrations: Matrix-based fitting

Similar to Hellmann et al. (2020), we find that the concentrations of MVEs in carbonaceous chondrites exhibit strong linear correlations with the matrix mass fractions (Fig. 1). The concentrations of MVEs in the non-matrix component derived from our fitting are reported along with previous data in Table 2. As expected, the concentrations show a decreasing trend with condensation temperature (Fig. 2), consistent with previous findings (Alexander, 2019; Hellmann et al., 2020). In contrast to Hellmann et al. (2020), who suggested that the non-matrix concentrations of MVEs with condensation temperatures lower than ~750 K all cluster around $(0.13 \pm 0.03)\times$CI chondrite values, our results

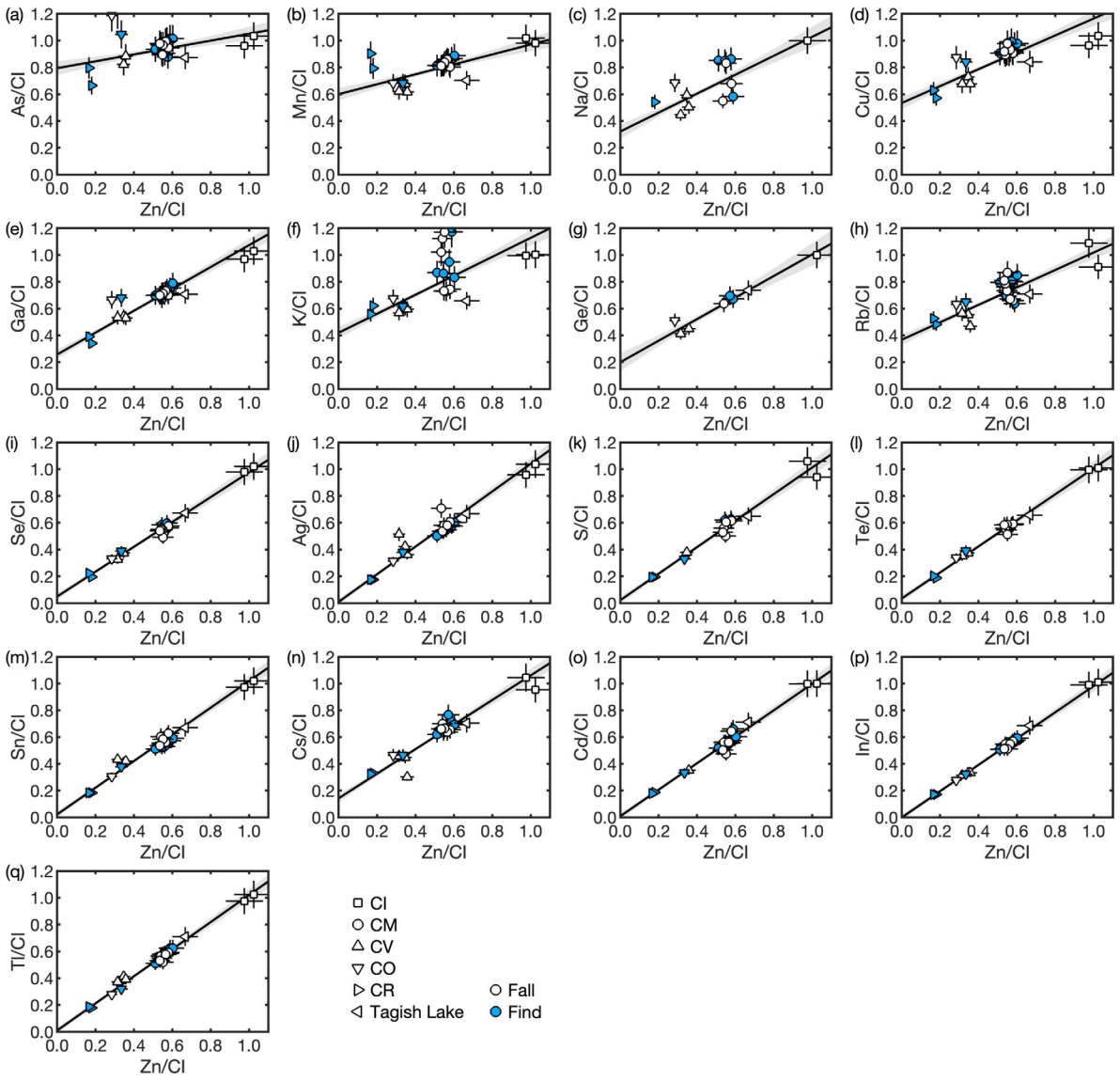

Fig. 4. MVE concentrations versus Zn concentrations of individual carbonaceous chondrite samples normalized by the CI chondrite values. The "fall" samples are shown in white, and the "find" samples are shown in light blue.

extend to much lower values (Fig. 2). For instance, our fits yield non-matrix concentrations of $2.1^{+3.8}_{-2.0}$ mg/g for S and 11^{+20}_{-10} μg/g for Zn (95% confidence intervals; for comparison, the values from Hellmann et al. (2020) are 6.5 ± 2.4 mg/g and 37 ± 15 μg/g), corresponding to CI-normalized values of $0.041^{+0.073}_{-0.038}$ and $0.030^{+0.059}_{-0.028}$, respectively (Figs. 2–3, Table 2). Although our inferred non-matrix MVE abundances differ systematically from those of Hellmann et al. (2020), they are strikingly similar to the "chondrule" component inferred by Alexander (2019) (Fig. 3).

3.2. MVE concentrations: Zn-based fitting

In general, the MVE and Zn concentrations exhibit good linear correlations. For the most volatile MVEs (Se, Ag, S, Te, Sn, Cs, Cd, In, and Tl), nearly all data points fall on straight lines (Figs. 4i–q). For other MVEs, especially Na (Fig. 4c) and K (Fig. 4f) in CM chondrites, the data exhibit notable scatter. The implications are discussed in Section 4.2.

Given an assumed Zn concentration for the non-matrix component, we can also infer the non-matrix MVE concentrations from the Zn-based fitting. If we assume a Zn concentration of 11 μg/g (from the matrix-based fitting), the inferred MVE concentrations agree very well with those obtained from the matrix-based fitting (Table 2, Fig. 5a). When higher Zn concentrations are assumed, the inferred non-matrix concentrations increase substantially for the most volatile MVEs, but only modestly for other elements (Fig. 5). If we assume a Zn concentration of 30 μg/g (which is close to the upper bound of the matrix-based confidence interval), the inferred concentrations of the most volatile MVEs also get close to the upper bounds of their respective matrix-based confidence intervals (Fig. 5d, in which the right ends of the x-axis error bars for the most volatile MVEs fall close to the 1:1 line). These results demonstrate the good consistency between the matrix- and Zn-based fittings, in terms of both best estimates and confidence intervals. Apparent discrepancies between the two approaches are observed for Na and Ge (Fig. 5), and they are discussed further in Section 4.2.

3.3. Isotopic compositions

Previous studies have demonstrated that δ correlate linearly with $1/c$ for Te, K, Rb, Zn, Cd, and Ge (Hellmann et al., 2020, 2023; Nie et al., 2021; Morton et al., 2024; Wölfer et al., 2025). We also include the data of Cu (Luck et al., 2003; Paquet et al., 2023) and Ga (Kato

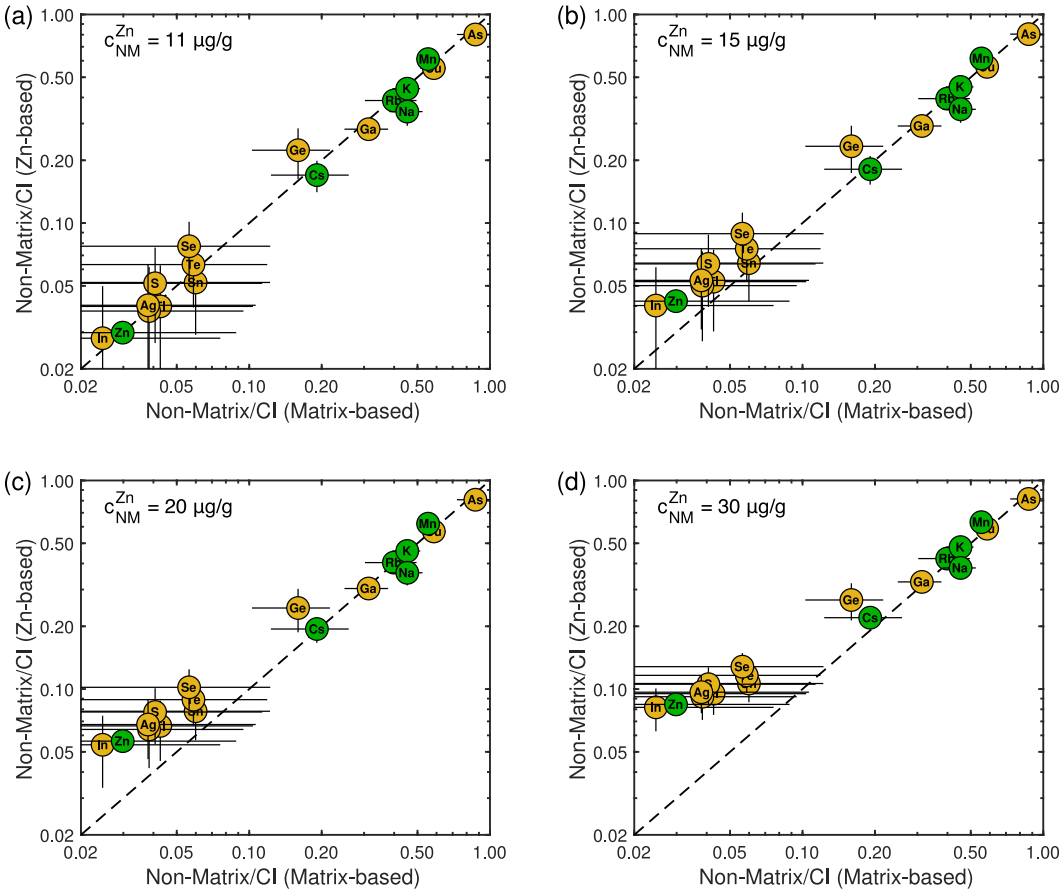

Fig. 5. Comparison of non-matrix MVE concentrations obtained from the matrix-based fitting and Zn-based fitting, under the assumptions of different non-matrix Zn concentrations (c^{Zn}_{NM}) within the confidence interval given by the matrix-based fitting.

and Moynier, 2017). We show the results in the δ-c space (Fig. 6) to illustrate the sensitivity of δ_{NM} to the uncertainty in c_{NM} (which is given in c rather than $1/c$), especially for Zn, Te, and Cd, although the fitting is done for the linear δ-$1/c$ relation. For Rb, Zn, Te, Ge, and Cu, the fitted relations well capture the δ-c relations (Fig. 6b,c,d,e,g). For K and Cd, the data show some scatter, but the overall trend is still well described by the fitted relation (Fig. 6a,f). For Ga, the data match the general trend that chondrites with low concentrations exhibit light isotopic signatures, but the data are not captured well by the fitted relation: The theoretical relation yields simultaneous changes in δ and c, while the data exhibit first variation in c but not δ from CI to CM, and then variation in δ but not c from CV to CO chondrites (Fig. 6h). This implies that more measurements are required to better describe the variations in Ga isotopic compositions among carbonaceous chondrites.

The fitted δ-c relations, together with the estimated c_{NM} values, lead to estimates of the non-matrix isotopic compositions, δ_{NM} (Fig. 6, Table 3), as well as the isotopic fractionations between the matrix and non-matrix components, $\Delta_{NM} = \delta_M - \delta_{NM}$ (Fig. 7, Table 3). (Here, we use the non-matrix concentrations and confidence intervals obtained from the matrix-based fitting, which yields broader confidence intervals for the isotopic compositions; further details of the calculations and uncertainty estimation are provided in Appendix D.) For K, Rb, and Ge, the δ_{NM} and Δ_{NM} values estimated here are similar to those from Nie et al. (2021) and Wölfer et al. (2025) (Fig. 7). For Zn, Te, and Cd, compared to previous studies (Hellmann et al., 2020; Nie et al., 2021; Morton et al., 2024), the δ_{NM} values are estimated to be much lower, and the fractionations Δ_{NM} are estimated to be much larger (Table 3, Fig. 7). Although these estimates have large uncertainties, the conclusion that the isotopic fractionations are substantially larger than previously inferred remains robust.

For Cu, the fractionation Δ_{NM} is estimated to be similar to those of Zn, Te, Ge, and Cd after normalization by relative isotopic mass difference (Fig. 7b). For Ga, taking the fitted result at face value, the inferred fractionation is moderate, smaller than those of Zn, Te, Cd, Cd, and Cu, but larger than those of K and Rb (Fig. 7b). However, given that the data do not conform closely to the theoretical trend of two-component mixing (Fig. 6h), the reliability of the inferred Ga isotopic composition and fractionation remains uncertain.

4. Discussion

4.1. Comparison with Hellmann et al. (2020) and Alexander (2019)

A key step in interpreting our results is to compare them with previous estimates of non-matrix MVE abundances derived by Hellmann et al. (2020) and Alexander (2019), which represent the two principal approaches to modeling carbonaceous chondrite compositions. We adopted the same overall framework as Hellmann et al. (2020), but with updated matrix mass fractions from Patzer et al. (2021, 2022, 2023). Our inferred non-matrix concentrations are systematically lower than those reported by Hellmann et al. (2020). For the most volatile MVEs (or the "plateau" elements, such as Zn and Te), our fits suggest non-matrix abundances of a few percent of the CI chondrite values (Fig. 2), much lower than those (~0.13×CI) reported by Hellmann et al. (2020) (Fig. 3a). The difference arises because the updated matrix mass fractions are higher than those applied by Hellmann et al. (2020) (Table 1). Increasing the matrix fraction would shift the data points rightward in the concentration versus matrix mass fraction plots (such as Fig. 1), which would in turn lower the y-axis intercepts of the fitted linear relations. This can be illustrated intuitively by considering an

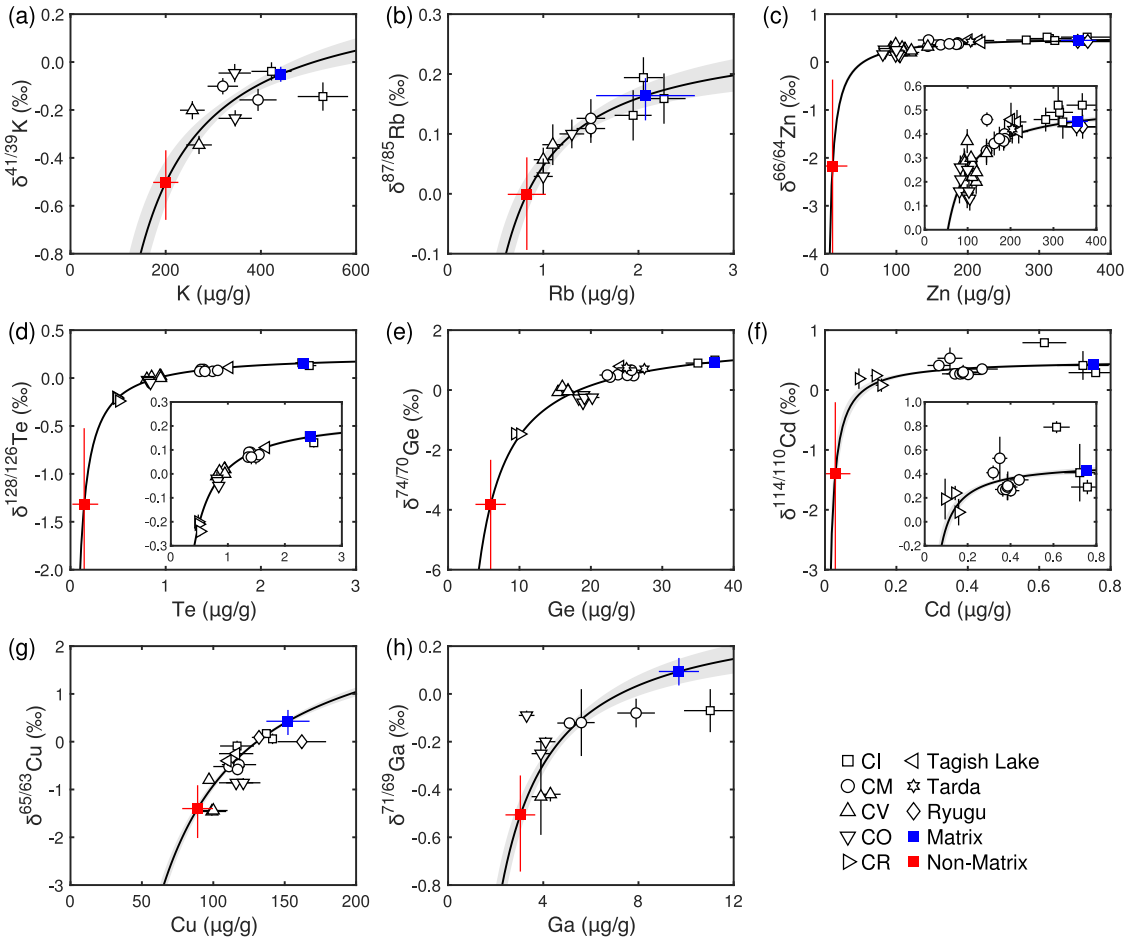

Fig. 6. The relationships between MVE concentrations and isotopic compositions for K (a), Rb (b), Zn (c), Te (d), Ge (e), Cd (f), Cu (g), and Ga (h). The black curves and gray areas are the best-fits and error envelopes obtained by fitting the linear relation between δ and $1/c$. The blue squares show the estimated matrix isotopic compositions according to the fitting results, which are in good consistency with the measured CI chondrite values (expect for Ga). The red squares show the estimated values of the non-matrix component.

end-member case: If an MVE has a near zero abundance in the non-matrix component, its CI-normalized abundance in a chondrite would basically reflect the matrix mass fraction. A chondrite with ~30 wt% matrix would show an abundance of ~30% the CI value for such an MVE. Conversely, if the matrix mass fraction is underestimated to be ~20%, the same bulk abundance would require a higher non-matrix abundance of ~10% of the CI chondrite value. As Hellmann et al. (2020) likely underestimated the matrix mass fractions of CM, CO, and CR chondrites by ~10% (Table 1), their model can be expected to yield a "plateau" of ~0.1×CI for the most volatile MVEs in the non-matrix component. The comparison of our results with those of Hellmann et al. (2020) highlights how matrix mass fractions strongly influence the inferred non-matrix MVE abundances.

In contrast, our results show much closer agreement with the "chondrule" component derived by Alexander (2019) (Fig. 3b). Strictly speaking, Alexander (2019) considered four components – chondrule, refractory inclusions, anhydrous matrix, and water. The anhydrous matrix and water together correspond to the matrix component in our model, while refractory inclusions are a minor component and basically MVE-free. Hence, for problems concerning MVEs, the chondrule component of Alexander (2019) effectively represents the non-matrix component. Although our predicted MVE abundances differ from those of Alexander (2019) for Ga, Ge, Ag, Te, and Sn (Table 2, Fig. 3b), these differences can be largely attributed to the different bulk chondrite group concentrations used in the fitting (Fig. 1e,g,k,m,n; to compare the chondrite compositions used in the two studies, one should focus on CM, CO, and CV chondrites, because we have introduced a sulfate oxygen correction for CI chondrites, and Alexander (2019) used the Renazzo values for CR chondrites).

Unlike this study and Hellmann et al. (2020), Alexander (2019) did not treat the mass fractions of the components as input data. Instead, they were optimized as fitting parameters to minimize the overall misfit in element concentrations. This approach avoids the uncertainties associated with matrix mass fractions. From this perspective, the close similarity between our results and those of Alexander (2019) provides independent support for the revised matrix mass fractions provided by Patzer et al. (2021, 2022, 2023).

4.2. *Insights from the Zn-based fitting*

The data reported by Braukmüller et al. (2018, 2019, 2025) include multiple CM samples that exhibit variations in all MVE concentrations. Understanding the origins of such variations is critical for proper interpretation and application of the data. The observation that the most volatile MVEs covary closely with Zn (Figs. 4i–q) suggests that these variations are primarily caused by differences in matrix mass fraction among the CM samples rather than measurement errors. In contrast, the alkali elements (Na, K, and Rb, though not necessarily Cs) in these CM chondrite samples do not correlate well with Zn (Figs. 4c,f,h), implying that the variations in alkalis among CM chondrites cannot be simply attributed to differing matrix mass fractions. Instead, they likely reflect parent-body aqueous alteration, which has also been invoked

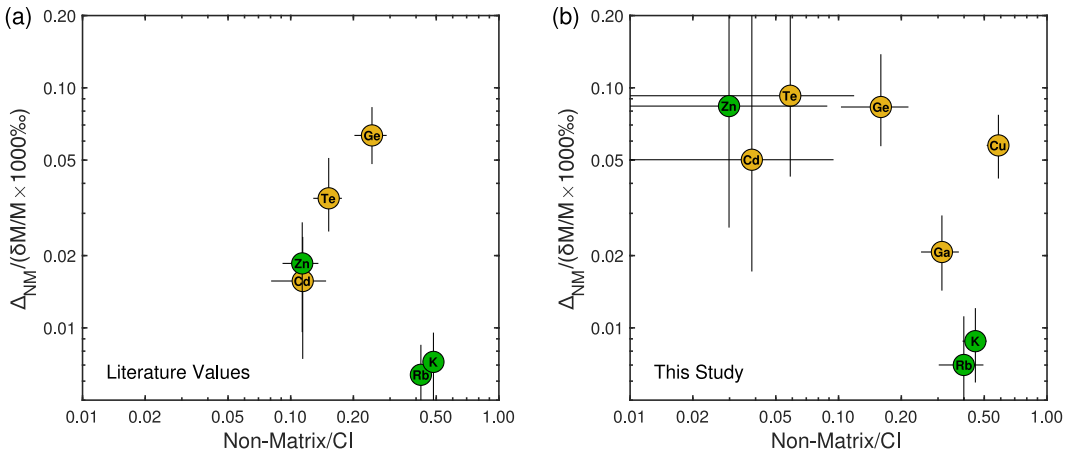

Fig. 7. The magnitudes of mass-dependent isotopic fractionations between the matrix and non-matrix components versus the non-matrix abundances of MVEs from the literature (Hellmann et al., 2020; Nie et al., 2021; Morton et al., 2024; Wölfer et al., 2025) (a) and this study (b). The abundances are normalized by the CI values, and the isotopic fractionations are normalized by the relative mass differences $\delta M/M$.

to explain the intra-group K isotopic variability (e.g., Jiang et al., 2021; Hu et al., 2024). Terrestrial modification may also contribute. Although "fall" samples show similar scatter with "find" samples (Figs. 4c,f,h), this does not necessarily rule out a terrestrial contribution. For example, rapid terrestrial alteration has been observed on timescales of days to months in the fall CM chondrite Winchcombe (Jenkins et al., 2024), including the formation of halite (NaCl). Such processes also introduce additional complexity in interpreting K isotopic variations among carbonaceous chondrites (see Appendix B).

In Figs. 4i–q, the data points of CV and CO chondrites almost entirely overlap, implying that the two groups of carbonaceous chondrites have nearly identical matrix mass fractions and thereby justifying our assumption for the matrix mass fraction of CV chondrites. The Tagish Lake sample lies close to the highest Zn concentration data point of the CM cluster, indicating that its matrix mass fraction is slightly higher than that of the most matrix-rich CM chondrite.

Regarding the non-matrix concentrations of MVEs, apparent discrepancies between the matrix- and Zn-based fittings are observed for Na and Ge (Fig. 5a, Table 2). These can be mostly attributed to the differences in the data used in the two fittings. For Na, several anomalous CM chondrite samples are excluded (Appendix B). In the matrix-based fitting, excluding these data points does not affect the x-axis data (matrix mass fraction), which are available only as group average. In the Zn-based fitting, the data points correspond to individual samples, and the x- and y-axis data are included or excluded simultaneously. For Ge, the samples measured by Wölfer et al. (2025) only partially overlap with those analyzed by Braukmüller et al. (2018). In the matrix-based fitting, all Ge data reported by Wölfer et al. (2025) are used to calculate group averages, whereas in the Zn-based fitting, only samples also measured by Braukmüller et al. (2018) can be included. In particular, no CR samples are included in the Zn-based fitting because the CR samples measured by Wölfer et al. (2025) and Braukmüller et al. (2018) do not overlap. In the matrix-based fitting, the CR data point lies below the fitted line (Fig. 1), implying that the inferred non-matrix abundance would likely increase if this point were excluded from the fitting. This is consistent with the result that the Zn-based fitting yields higher non-matrix Ge concentrations (Fig. 5). The discrepancies observed for Na and Ge further emphasize the importance of data consistency.

The inter-correlation between estimates of different MVEs (Fig. 5) may also provide a way to more tightly constrain non-matrix MVE concentrations if some of the most volatile MVEs can be limited to a narrower interval than that given by the matrix based fitting. Considering the correlation between the concentration of Zn and those of organic C and presolar grains (which occur exclusively in the matrix component with nearly constant abundances), Alexander (2019) suggested that the non-matrix concentration of Zn is close to zero. This implies that the lower values (e.g., 11 μg/g) should be more relevant than the higher values (e.g., 30 μg/g).

Additional constraints may be provided by measurements of chondrules. Kong and Palme (1999) measured Zn concentrations of chondrules and matrix in the CR chondrite Renazzo. The chondrules show large variations in Zn concentration, with a mass-weighted average of approximately 30 μg/g. This value has likely been affected by aqueous alteration in the parent body, which redistributed elements between matrix and chondrules (as can be expected from the general effects of chondrule-matrix exchange; e.g., Grossman and Brearley, 2005; Alexander, 2019). The pre-alteration value was almost certainly lower. The reported Zn concentration in the matrix (~250 μg/g) is substantially lower than the CI chondrite value (~350 μg/g; Table 2), implying that a significant portion of Zn that was originally in the matrix migrated into the chondrules. Among the measured chondrules, those with K concentrations of ≲200 μg/g (i.e., comparable to our inferred non-matrix value and therefore likely affected least by aqueous alteration) exhibit Zn concentrations of ≲15 μg/g, close to the matrix-based best estimate, 11 μg/g.

Patzer et al. (2022) reported S concentrations in chondrules of multiple CR chondrites, with an average value of 4.0 mg/g. If the value from EET 92042 chondrules (6.2 mg/g), which is substantially higher than those in chondrules of other CR samples, is excluded, the average decreases to 3.5 mg/g, which corresponds to 0.067 times the CI chondrite value and is consistent with the Zn-based fitting assuming a Zn concentration of ~15 μg/g (Fig. 5b). This value may effectively represent the non-matrix component, as contributions from refractory inclusions and isolated grains are negligible (Patzer et al., 2022). As previously discussed for Zn, this value has likely been influenced by aqueous alteration and S redistribution, and the original concentration was almost certainly lower. If the above arguments are valid, the Zn concentration of the non-matrix component can be constrained to be lower than ~15 μg/g, and the estimates based on the assumption of 11 μg/g Zn given in Fig. 5a and the last column of Table 2 (with fairly narrow confidence intervals) can be considered reasonable.

4.3. Isotopic fractionations between matrix and non-matrix components

For K, Rb and Ge, the isotopic fractionations estimated in this study are similar to the values suggested by previous studies (Nie et al., 2021; Wölfer et al., 2025), whereas for Zn, Te, and Cd, the isotopic fractionations estimated here are much larger than the previous estimates (Hellmann et al., 2020; Nie et al., 2021; Morton et al., 2024) (Fig.

7). These differences in isotopic fractionations are caused by those in the estimated abundances of the MVEs. In general, we estimate lower non-matrix MVE abundances than previous studies using the matrix mass fractions from Hellmann et al. (2020) (Fig. 3a). As δ_{NM} correlates positively with c_{NM} (Fig. 6), the isotopic compositions of the non-matrix component estimated here are generally lighter than previously suggested. For K, Rb, and Ge, this effect is limited because their non-matrix concentrations (after CI-normalization) are relatively high, and the sensitivity of δ_{NM} to c_{NM} is correspondingly weak (Fig. 6). For Zn, Te, and Cd, our estimates shift the value into a regime where δ_{NM} is highly sensitive to c_{NM}, and thus estimated fractionations become much larger. Although the estimated isotopic compositions are associated with large uncertainties (due to the extreme sensitivity of δ_{NM} to c_{NM} and the limited ability of the c-f regression to precisely constrain c_{NM}), the conclusion remains robust that the isotopic fractionations are substantially larger than previously inferred.

It is instructive to compare our estimates with measurements of carbonaceous chondrite components. For example, Zn isotopic compositions have been measured in CV chondrite components (Pringle et al., 2017; van Kooten and Moynier, 2019; van Kooten et al., 2021). van Kooten et al. (2021) reported that the Zn isotopic compositions of the "cores" of chondrules in Leoville (a weakly altered sample) are ~1.3‰ lighter than those of CI chondrites. This measured composition is heavier than our best estimate for δ_{NM}, but lighter than the upper bound of its confidence interval (which are ~2.6‰ and ~0.8‰ lighter than CI, respectively; Table 2). It is noteworthy that the igneous rims of the chondrules have heavier Zn isotopic compositions (van Kooten and Moynier, 2019; van Kooten et al., 2021), implying that bulk chondrules would exhibit an even smaller isotopic fractionation. This comparison between the direct measurements and our estimate may indicate either that the actual fractionation is closer to the lower end of our estimated confidence interval, or that the chondrules were shifted toward heavier Zn isotopic compositions through chondrule-matrix exchange (Grossman and Brearley, 2005; Alexander, 2019). Meanwhile, the measured Zn isotopic compositions of the CV matrix are close to but lighter than the CI value (Pringle et al., 2017; van Kooten and Moynier, 2019; van Kooten et al., 2021). This may imply that both chondrules and matrix were modified, and the chondrule-matrix exchange may at least partly account for the deviation between our preferred estimate and the direct measurements. Evidence for significant exchange exists even in the least altered samples, particularly for oxygen isotopes (Kita et al., 2010) and alkali elements (Grossman and Brearley, 2005). Despite this potential complexity, petrological constraints on chondrite components remain critical for understanding the inferred elemental and isotopic compositions of the non-matrix component. For example, observations of diffusion profiles in metal grains (Humayun, 2012) and relict grains in chondrules (Jones, 2012) provide important insights into the mechanisms for the isotopic fractionations, as discussed in the following subsection.

4.4. Possible mechanisms of the inferred isotopic fractionations

Having estimated the isotopic fractionations between the matrix and non-matrix components, a natural question is their origin: Do these fractionations reflect chondrule formation or were they inherited from chondrule precursors? For K and Rb, Nie et al. (2021) demonstrated that the fractionations can be explained by re-condensation under reasonable conditions during chondrule cooling. For Zn, Te, Cd, Ge, and Cu, the fractionations are much larger (Fig. 7b), and it remains unclear whether they can be explained by re-condensation alone. Nevertheless, another mechanism may also play a role during the re-condensation of these elements: diffusion from the surfaces into the interiors of chondrules or metal grains (Alexander, 2005; Alexander et al., 2022).

The role of diffusion can be understood as follows: During cooling, MVEs in the gas condense onto the surfaces of chondrules or metal grains. Without diffusion into the interior, the condensed elements would accumulate at the surface, increasing their surface concentrations and thus the equilibrium vapor pressure, which would inhibit further condensation (Alexander, 2005; Alexander et al., 2022). K and Rb condense at relatively high temperatures and have relatively high diffusion coefficients (e.g., Zhang et al., 2021). As a result, the diffusion of these two elements can be sufficiently rapid that isotopic fractionation is primarily controlled by the re-condensation process (Jacquet et al., 2026), consistent with the assumption of Nie et al. (2021). However, for other elements, the effects of diffusion can be much greater.

Cu, Ga, and Ge are siderophile MVEs, and they condense mostly into metal. In carbonaceous chondrite chondrules that are strongly depleted in sulfur, metal is expected to solidify early during cooling, at temperatures near the melting point of Fe (~1800 K). Thus, Cu, Ga, and Ge that condense below that temperature need to diffuse into grains of solid metal. In this case, the overall condensation is controlled by the slow solid-state diffusion, as implied by the diffusion profiles of Cu and Ga preserved in CR chondrite metal grains (Humayun, 2012). Zn likely behaves as a lithophile MVE and condenses into silicate melts during chondrule cooling (Singerling et al., 2021). However, compared with K and Rb, Zn exhibits stronger volatility and condenses at lower temperatures (e.g., Sossi et al., 2019). Moreover, Zn is a divalent cation and therefore diffuses more slowly than monatomic cations such as K and Rb in silicate melts at given temperature (Zhang et al., 2010). For these two reasons, the diffusion of Zn during its condensation can be expected to be much slower than that of K and Rb. Hence, for the lithophile Zn, the overall rate of condensation during chondrule cooling may also be controlled by the diffusion step.

The process of diffusion can lead to significant isotopic fractionation. As an illustration, we consider the simplest example of diffusion from a surface with fixed concentration into a half-space with zero initial concentration. If the diffusion coefficient is D and the diffusion time is t, the integrated diffusive flux is proportional to $\sqrt{Dt}$. For two isotopes i and j with diffusion coefficients D_i and D_j, the ratio of their integrated fluxes is $\sqrt{D_i/D_j}$, and the fractionation factor is $\Delta = 1000‰ \times (\sqrt{D_i/D_j} - 1)$. Assuming a mass dependence of diffusion coefficient described by $D_i/D_j = (M_j/M_i)^{\beta}$, where M_i and M_j are the masses and β is a coefficient (e.g., Richter et al., 1999, 2009; Watkins et al., 2017), we write the fractionation factor as $\Delta = 1000‰ \times ((M_j/M_i)^{\beta/2} - 1) \approx 1000‰ \times (\delta M/M)(\beta/2)$, in which $\delta M/M = (M_j - M_i)/M_i$ is the relative mass difference. The diffusion into chondrules or metal grains during chondrule cooling is more complicated than this extreme example, but the maximum fractionation induced by diffusion can still be expected to be $\Delta \approx 1000‰ \times (\delta M/M)(\beta/2)$. The coefficient β varies with the diffusing element and the system. In silicate melts, β can be up to ~0.2, while in metals, β can be up to ~0.4 (Richter et al., 2009; Watkins et al., 2017). Thus, in principle, for lithophile and siderophile elements, the fractionations after normalization by the relative mass difference can be up to ~0.1 and ~0.2, respectively. We note that our calculations oversimplify the kinetic processes of MVE recondensation during chondrule cooling. This is particularly important in the context of petrological observations (e.g., the presence of relict grains) which suggest that some chondrules underwent multiple melting events (e.g., Jones, 2012), such that their isotopic compositions may represent cumulative results of repeated fractionations. However, regardless of the details, the end-member calculations suggest that the relatively large isotopic fractionations inferred from our fitting (Fig. 7) may possibly be explained by diffusion in chondrules and metal grains during re-condensation upon chondrule cooling.

4.5. Origin of volatile depletion in chondrules

The origin of volatile depletion in chondrules holds important implications for the long standing problem of chondrule formation. Hellmann et al. (2020) suggested a ~0.13×CI "plateau" for MVEs with 50%

condensation temperatures lower than ~750 K in the non-matrix (chondrule) component of carbonaceous chondrites. The authors argued that this "plateau" requires bulk condensation of a gas with CI-like relative proportions of these elements. In this case, the process of chondrule formation does not cause elemental or isotopic fractionation, and the compositions of chondrules largely reflect those of their precursors.

In this study, we suggest that the "plateau" is likely an artifact of their underestimated matrix mass fractions, as discussed in Section 4.1. Our revised non-matrix composition exhibits substantial variation in the CI-normalized concentrations of these elements (Figs. 2, 3, and 5a). The concentrations of these elements do not show clear correlation with their 50% condensation temperatures. However, this is probably because the 50% condensation temperature describes the behaviors of elements in the canonical nebular environment rather than the chondrule-forming environment. As discussed in Section 4.3, the isotopic compositions of the non-matrix component may be explained by mass-dependent fractionation processes during chondrule formation. Therefore, we suggest that the elemental and mass-dependent isotopic compositions of MVEs in carbonaceous chondrite chondrules may be explained by chondrule formation without invoking inheritance from chondrule precursors, although more detailed investigations are certainly required to test this hypothesis.

5. Conclusions

In this study, we re-assess the concentrations of MVEs in the non-matrix component of carbonaceous chondrites. We update the matrix mass fractions using the measurements reported by Patzer et al. (2021, 2022, 2023) and fit the relations between MVE abundances and matrix mass fractions across the carbonaceous chondrite groups. The revised MVE abundances in the non-matrix component are broadly consistent with those inferred by Alexander (2019), but systematically lower than the estimates of Hellmann et al. (2020). Unlike Hellmann et al. (2020), who inferred a ~13% CI chondrite level "plateau" for elements with condensation temperatures lower than ~750 K, our results suggest lower abundances (e.g., a few percent of the CI chondrite values) for these elements in the non-matrix component.

In addition to the concentration-matrix mass fraction relations, we also examine the correlations between the concentrations of Zn and other MVEs. This practice provides useful insights into the data and the fitting results. The almost perfect correlation of the most volatile MVEs with Zn indicates that the significant intra-group variations among the CM chondrites reported by Braukmüller et al. (2018) can primarily be attributed to differing matrix mass fractions. Nevertheless, the scattered results for alkalis (especially Na and K) imply that they were affected by either parent-body alteration or terrestrial modifications. Assuming non-matrix Zn concentrations within the matrix-based confidence interval, we also infer the non-matrix abundances of MVEs from this Zn-based fitting. The comparison between the matrix- and Zn-based fittings illustrates good consistency for most elements in terms of both the best estimate and the confidence interval. Apparent discrepancies are observed for Na and Ge, for which the samples included in the calculation of group-average concentrations differ from those of other MVEs due to data availability or exclusion of anomalous data. This further demonstrates the importance of data self-consistency.

The revised non-matrix (or chondrule) abundances of MVEs have profound implications for both chondrule formation and planetary accretion. By combining the revised estimates of non-matrix MVE abundances with existing isotopic data, we obtain new constraints on isotopic compositions of the non-matrix component. While the results for K, Rb, and Ge compare well with previous studies, our inferred fractionations (between matrix and non-matrix components) for Zn, Te, and Cd are substantially larger than previously estimated. This is because our re-assessment suggests much lower abundances for these elements in the non-matrix component. Considering the origin of these inferred isotopic compositions, we suggest they may be explained by the fractionations associated with the diffusion of these MVEs from the surfaces to the interiors of chondrules or metal grains upon their re-condensation during the cooling stage of chondrule formation. This possible explanation, together with the newly revised, non-uniform CI-normalized concentrations of the most volatile MVEs, implies that the MVE abundances and isotopic compositions of chondrules may be attributed to chondrule formation alone without invoking precursor signatures.

Table 3
The inferred values and 95% confidence intervals of the isotopic compositions of the non-matrix component (δ_{NM}) and the fractionations and between matrix and non-matrix components (Δ_{NM}) for K, Rb, Zn, Te, Ge, Cd, Cu, and Ga.

	δ_{NM}	95% c.i.	Δ_{NM}	95% c.i
K	−0.50	(−0.68, −0.34)	0.45	(0.30, 0.62)
Rb	0.00	(−0.10, 0.07)	0.16	(0.10, 0.26)
Zn	−2.17	(−14.8, −0.35)	2.62	(0.82, 15.3)
Te	−1.32	(−7.69, −0.52)	1.47	(0.68, 7.84)
Ge	−3.82	(−6.95, −2.33)	4.75	(3.26, 7.89)
Cd	−1.40	(−17.3, −0.14)	1.82	(0.62, 17.7)
Cu	−1.40	(−2.03, −0.90)	1.83	(1.33, 2.45)
Ga	−0.51	(−0.75, −0.33)	0.60	(0.41, 0.85)

Notes: The isotopic compositions and fractionations are given in ‰. For Zn, Te, and Cd, the upper limit of fractionation is taken as the theoretical value of pure kinetic condensation, $\Delta = 1000‰ \times |\sqrt{M_j/M_i} - 1|$, where M_i and M_j are the masses of the heavy and light isotopes.

CRediT authorship contribution statement

Zhongtian Zhang: Writing – original draft, Visualization, Validation, Methodology, Investigation, Formal analysis, Conceptualization. **Damanveer S. Grewal:** Writing – review & editing, Validation, Methodology, Investigation, Conceptualization.

Declaration of Generative AI and AI-assisted technologies in the writing process

During the preparation of this work, the authors used ChatGPT in order to assist with minor editing of some sentences. After using this tool, the authors reviewed and edited the content as needed and take full responsibility for the content of the publication.

Declaration of competing interest

The authors declare that they have no known competing financial interests or personal relationships that could have appeared to influence the work reported in this paper.

Acknowledgments

We thank Conel Alexander, Nicole Nie, and Jinghao Sun for helpful discussions, two anonymous reviewers for their constructive comments, and the associate editor Paolo Sossi for efficient handling of the manuscript. This study was supported by the Harry Hess Fellowship from Princeton University to Z.Z. and the startup funds from Yale University to D.S.G..

Appendix A. Matrix mass fractions

In Hellmann et al. (2020), the matrix mass fractions were estimated from previously reported component volume fractions, previously reported chondrite bulk densities, and assumed densities of chondrule, metal, sulfide, and refractory inclusions (but not matrix). The results provided good first-order approximations of the matrix mass fractions, but are prone to problems from several factors, such as (i) intra-group variations in component volume fractions and bulk chondrite densities, which may be measured from different samples, (ii) errors

in assumed component densities or variations in component densities among different groups or different samples within the same group, and (iii) inconsistent definitions of "component volume fractions" across different studies. We take CR chondrites as an example to discuss these issues. (i) CR chondrites exhibit significant variations in bulk density (Macke et al., 2011) and component volume fractions (Schrader et al., 2011), and taking group-average values from different studies (which may be based on different samples) could lead to errors. (ii) The densities of chondrite components, as demonstrated by Patzer et al. (2021, 2022, 2023) vary among chondrite samples, and they may not be accurately described by fixed values. (iii) Hellmann et al. (2020) obtained a particularly low matrix mass fraction for the CR group largely because they adopted a quite large volume fraction (~10 vol%) of metal, which was considered part of the non-matrix component. The measurements of Schrader et al. (2011) (the source cited by Hellmann et al. (2020) for CR component volume fractions) suggested ~10 vol% opaque minerals, and that value includes oxide, rust, metal, and sulfide (instead of just metal). Howard et al. (2015) determined the modal mineralogy of CR chondrite samples and reported metal fractions of ~3–7 vol%, with an average of ~5 vol%. Therefore, the matrix mass fraction for CR chondrites has likely been underestimated.

Other attempts to estimate matrix mass fractions indeed resulted in higher values. Bryson and Brennecka (2021) assumed that the grain density (i.e., porosity-free density) of the matrix is the same as that of the non-matrix component and obtained a matrix mass fraction of ~29% for CR chondrites. However, this value is still very assumption-dependent. So far, the most robust estimates are provided by Patzer et al. (2021, 2022, 2023), which carefully examined the volume fractions and detailed mineral compositions of each component for CM, CO, and CR chondrites. For these three groups, we estimate the average matrix mass fractions from the values reported for individual samples (specifically, the values from "corrected for mixed analyses") by Patzer et al. (2021, 2022, 2023), and evaluate the uncertainties by calculating their two standard deviations. For CMs and COs, the values reported for individual samples exhibit moderate intra-group variations, with ranges of 51–62% for CMs and 26–37% for COs. For these two groups, we include all samples in the calculation.

Among the CR chondrite samples studied by Patzer et al. (2022), the matrix mass fraction varies from 13% to 35%, and the S content varies from 0.86 wt% to 1.65 wt%. Patzer et al. (2022) did not measure Zn contents, but measurements from previous studies (Kallemeyn and Wasson, 1982; Kong et al., 1999; Hewins et al., 2014) for meteorites used in the Patzer et al. (2022) analyses suggested a variation from less than ~60 μg/g to ~100 μg/g. This large intra-group variation warrants additional caution when estimating the group average, especially because we need to combine data (matrix mass fraction and concentrations) from different sources; self-consistency is critical in this process. In the two CR samples analyzed by Braukmüller et al. (2018, 2019), the S and Zn concentrations are ~1.0 wt% and ~60 μg/g, respectively. Patzer et al. (2022) examined six CR samples, EET 92042, MET 00426, MIL 090657, QUE 99177, and two sections of Renazzo. MIL 090657 and QUE 99177 exhibit similar matrix mass fractions (15.1% and 13.1%) and S contents (0.94 wt% and 0.86 wt%), which are both lower than ~1.0 wt% but close. EET 92042 and MET 00426 exhibit almost identical matrix mass fractions (19.6% and 20.5%). Their S contents (1.46 wt% and 1.29 wt%) are both higher than 1.0 wt%, but the Zn content of EET 92042 (~61 μg/g; Kong et al., 1999) is almost identical to the values (~60 μg/g) reported by Braukmüller et al. (2018). Renazzo, in contrast, exhibits S content (~1.6 wt%; Patzer et al., 2022) and Zn content (~100 μg/g; Kallemeyn and Wasson, 1982; Hewins et al., 2014) substantially higher than the values reported by Braukmüller et al. (2018, 2019). Therefore, we exclude the two Renazzo sections from the average-CR matrix mass fraction estimate.

The matrix mass fraction of CV chondrites may also be problematic. This is because: (i) as discussed in Section 2.1, there is not yet a detailed matrix mass fraction estimate equivalent to those of Patzer et al. (2021, 2022, 2023); and (ii) CV chondrites include oxidized and reduced subgroups and exhibit a relatively wide range in matrix volume fraction (e.g., Gattacceca et al., 2020) and MVE concentrations (e.g., Wasson et al., 2013). The measurements of Braukmüller et al. (2018) include three CV samples: two pieces of Allende (CV-oxidized) and one piece of Vigarano (CV-reduced). Although these samples belong to different subgroups, their MVE concentrations differ only slightly. For example, their Zn concentrations only range from 112 μg/g for Vigarano to 123 μg/g and 127 μg/g for the two Allende samples. In general, as shown in Fig. 4 (where individual samples are plotted) and in the data compiled in the Supplementary Material, the CV chondrite samples included in our fitting exhibit limited variability, and their MVE concentrations broadly overlap with those of CO samples (although the CV–CO comparison varies among different MVEs). Therefore, we suggest that, for the dataset employed in the present study, it is sufficient to retain the estimate of $30.5 \pm 7.3\%$ from Hellmann et al. (2020), which closely matches the updated CO value ($31.1 \pm 11.0\%$). However, this may not hold for future studies if additional CV measurements with greater variability are included. This highlights the need for more investigations of CV chondrites.

Appendix B. Elemental and isotopic compositions

To maximize the internal consistency of the data, we take most of the concentration data from Braukmüller et al. (2018), including the concentrations of Na, K, Mn, Cu, Zn, Ga, As, Rb, Ag, Cd, In, Sn, Cs, and Tl. For S, Se, and Te, we take the data from Braukmüller et al. (2019, 2025), although they were also reported by Braukmüller et al. (2018), because the later measurements have better precisions. For Ge, we take the data from Wölfer et al. (2025) because this element was not included in the Braukmüller et al. (2018) measurements. Some data are apparently anomalous. For example, the Na concentrations of CM samples Murray, Murchison, EET 96029, LON 94102, SCO 06043, and MET 01070 are lower than those of other CM samples by approximately a factor of two or more. These anomalous data are excluded. The concentration data used in the fitting are listed in Table S2. For S, Se, Te, and Ge, fewer data points are shown in Fig. 4 because the subsequent studies measured fewer samples than Braukmüller et al. (2018). The Ge data from Wölfer et al. (2025) are paired with the Zn data from Braukmüller et al. (2018) if the measurements were from samples of the same meteorites. In the MVE versus Zn fitting, the two-standard-deviation uncertainties are uniformly assumed to be 10% of the reported concentrations. Repeated measurements of the Ivuna sample by Braukmüller et al. (2018) indicate that relative uncertainties vary among different elements, and the value adopted here is close to the upper bound of those reported uncertainties.

In this study, we consider the isotopic variations of K, Rb, Zn, Te, Ge, Cd, Cu, and Ga. We use data of K and Rb from Nie et al. (2021) (see below for discussion), Zn from Luck et al. (2005), Pringle et al. (2017), and Paquet et al. (2023), Te from Hellmann et al. (2020), Ge from Wölfer et al. (2025) and Luais and Florin (2025), Cd from Baker et al. (2010) and Morton et al. (2024), Cu from Luck et al. (2003) and Paquet et al. (2023), and Ga from Kato and Moynier (2017). For Cd, we only include data from the CI, CM, and CR groups, because the elemental and isotopic compositions of Cd can be easily affected by thermal metamorphism (Morton et al., 2024). All these studies reported concentrations and isotopic compositions simultaneously, so internal consistency is naturally guaranteed. The two-standard-deviation uncertainties of the concentrations are assumed to be 10% the reported values if the uncertainties were not reported together with the measurements. The data are given in Tables S3–S10.

The abundances and isotopic compositions of K exhibit significant intra-group variations, likely due to parent-body aqueous alteration (e.g., Jiang et al., 2021; Hu et al., 2024) or perhaps terrestrial modification. Even within the same meteorite samples, such as Ivuna (CI), Murchison (CM), and Allende (CV), substantially different values

have been reported (e.g., Jiang et al., 2021; Hu et al., 2024). The elemental and isotopic variations caused by aqueous alteration are not expected to follow the δ-c relationship derived from a two-component mixing model, and their influence should be minimized. To determine pre-alteration K abundances and isotopic compositions in carbonaceous chondrites is challenging and beyond the scope of this study. To facilitate comparison with previous results and to isolate the effect of our revised non-matrix abundances, we adopt the same K (and Rb) dataset as Nie et al. (2021).

Appendix C. York fitting and posterior parameter distribution

Here, we briefly describe the York method for fitting a linear relation with errors in both coordinates (York et al., 2004). Assuming that we have N data points (X_i, Y_i) associated with uncertainties expressed as standard deviation $(\sigma_{X,i}, \sigma_{Y,i})$, and the errors in X and Y are uncorrelated. The two variables are expected to follow a linear relation

$$Y = \omega X + \theta. \tag{C.1}$$

In this case, the estimated values of ω and θ are expected to follow

$$\mu_\omega = \left(\sum_{i=1}^{N} W_i \Gamma_i V_i\right)\left(\sum_{i=1}^{N} W_i \Gamma_i U_i\right)^{-1}, \tag{C.2}$$

$$\mu_\theta = \bar{Y} - \mu_\omega \bar{X}, \tag{C.3}$$

where μ_ω and μ_θ are the estimated values of ω and θ, and W_i, $\bar{X}$, $\bar{Y}$, U_i, V_i, and Γ_i are defined as

$$W_i = \left(\sigma_{Y,i}^2 + \mu_\omega^2 \sigma_{X,i}^2\right)^{-1}, \tag{C.4}$$

$$\bar{X} = \left(\sum_{i=1}^{N} W_i X_i\right)\left(\sum_{i=1}^{N} W_i\right)^{-1}, \quad \bar{Y} = \left(\sum_{i=1}^{N} W_i Y_i\right)\left(\sum_{i=1}^{N} W_i\right)^{-1}, \tag{C.5}$$

$$U_i = X_i - \bar{X}, \quad V_i = Y_i - \bar{Y}, \tag{C.6}$$

$$\Gamma_i = W_i\left(\sigma_{Y,i}^2 U_i + \mu_\omega \sigma_{X,i}^2 V_i\right). \tag{C.7}$$

Particularly, W_i represents the weight of data point (X_i, Y_i), $\bar{X}$ and $\bar{Y}$ are weighted averages of X and Y data, U_i and V_i describe the difference between the data point and the weighted averages, and Γ_i gives the difference between the "adjusted" X value (see below for details) and $\bar{X}$. Because W_i, $\bar{X}$, $\bar{Y}$, U_i, V_i, and Γ_i depend on μ_ω, Eqs. (C.2) and (C.3) are not explicit expressions of μ_ω and μ_θ. Hence, the values of μ_ω and μ_θ need to be solved with an iterative scheme. After obtaining the values of μ_ω and μ_θ, their variance and covariance can be calculated as

$$\sigma_\omega^2 = \left(\sum_{i=1}^{N} W_i(\Gamma_i - \bar{\Gamma})^2\right)^{-1}, \tag{C.8}$$

$$\sigma_\theta^2 = (\bar{X} + \bar{\Gamma})^2\left(\sum_{i=1}^{N} W_i(\Gamma_i - \bar{\Gamma})^2\right)^{-1} + \left(\sum_{i=1}^{N} W_i\right)^{-1}, \tag{C.9}$$

$$\sigma_{\omega,\theta} = -(\bar{X} + \bar{\Gamma})\left(\sum_{i=1}^{N} W_i(\Gamma_i - \bar{\Gamma})^2\right)^{-1}, \tag{C.10}$$

where $\bar{\Gamma} = (\sum_{i=1}^{N} W_i \Gamma_i)/(\sum_{i=1}^{N} W_i)$ is the weighted average of Γ_i.

The above results can be derived both from the least-squares method and the maximum-likelihood method (York et al., 2004). In the maximum-likelihood method, the results are obtained by maximizing the likelihood function $\mathcal{L}$ given by Titterington and Halliday (1979)

$$\ln \mathcal{L} = \mathcal{K} - (1/2)\chi^2, \tag{C.11}$$

where $\mathcal{K}$ is a constant, and χ^2 is expressed as

$$\chi^2 = \sum_{i=1}^{N}\left[\left(\frac{x_i - X_i}{\sigma_{X,i}}\right)^2 + \left(\frac{\omega x_i + \theta - Y_i}{\sigma_{Y,i}}\right)^2\right], \tag{C.12}$$

where x_i is the true X value of the i-th data point, whose observed value is X_i. The likelihood function can be derived under the assumption that (i) the deviations between the observed values, X_i and Y_i, and the true values x_i and $y_i = \omega x_i + \theta$, follow normal distributions with standard deviations $\sigma_{X,i}$ and $\sigma_{Y,i}$, and (ii) the errors in the two variables are uncorrelated, such that $x_i - X_i \sim \mathcal{N}(0, \sigma_{X,i}^2)$ and $\omega x_i + \theta - Y_i \sim \mathcal{N}(0, \sigma_{Y,i}^2)$. (In general, $\xi \sim \mathcal{N}(\mu_\xi, \sigma_\xi^2)$ means that variable ξ follows a normal distribution with mean μ_ξ and standard deviation σ_ξ.) In this case, the likelihood function is basically the joint probability distribution function of the data conditional on the model, and $\mathcal{K} = -(1/2)\sum_{i=1}^{N}\left[\ln(2\pi\sigma_{X,i}^2) + \ln(2\pi\sigma_{Y,i}^2)\right]$. To maximize $\mathcal{L}$, one needs to minimize χ^2. For given ω and θ, the minimum χ^2 is obtained when $\partial\chi^2/\partial x_i = 0$, which is obtained when x_i takes the value of

$$\tilde{x}_i = \bar{X} + \Gamma_i, \tag{C.13}$$

where $\tilde{x}_i$ is the adjusted value of X_i, and $\bar{X}$ and Γ_i are given by Eqs. (C.5) and (C.7) if μ_ω and μ_θ are considered as ω and θ (Titterington and Halliday, 1979; York et al., 2004). Substituting $x_i = \tilde{x}_i$ into Eq. (C.12), the expression of χ^2 becomes

$$\tilde{\chi}^2 = \sum_{i=1}^{N} \frac{(\omega X_i + \theta - Y_i)^2}{\sigma_{Y,i}^2 + \omega^2 \sigma_{X,i}^2}, \tag{C.14}$$

where $\tilde{\chi}^2$ is the "plug-in" value of χ^2. As shown in Titterington and Halliday (1979) and York et al. (2004), $\tilde{\chi}^2$ is minimized at $\omega = \mu_\omega$ and $\theta = \mu_\theta$ with μ_ω and μ_θ given by Eqs. (C.2)–(C.7).

The uncertainties of the parameters should be characterized by their posterior probability distributions, i.e., the probability distributions conditional on the data. In Bayesian statistics, the posterior probability is proportional to the product of the prior and the likelihood. If we take $x_i = \tilde{x}_i$ to evaluate the likelihood, the posterior of (ω, μ) is expressed as

$$\phi(\omega, \theta) = C p(\omega, \theta)\tilde{\mathcal{L}}(\omega, \theta), \tag{C.15}$$

where $\phi(\omega, \theta)$ and $p(\omega, \theta)$ are the posterior and prior probability distribution functions of (ω, θ), C is a normalizing factor, and $\tilde{\mathcal{L}}$ is the "plug-in" likelihood,

$$\ln \tilde{\mathcal{L}}(\omega, \theta) = \mathcal{K} - (1/2)\tilde{\chi}^2, \tag{C.16}$$

In the standard fitting, there are no prior constraints, and $p(\omega, \theta)$ can be considered constant (or broad enough so that it is effectively constant when ω and μ are not extremely far from the μ_ω and μ_θ). At (μ_ω, μ_θ), which leads to maximum likelihood, $\partial \ln \mathcal{L}/\partial\omega = \partial \ln \mathcal{L}/\partial\theta = 0$. In the vicinity of (μ_ω, μ_θ), $\ln \mathcal{L}$ can be approximated using a Taylor expansion as the sum of $\ln \mathcal{L}(\mu_\omega, \mu_\theta)$ and a quadratic term in $(\omega - \mu_\omega, \theta - \mu_\theta)$. With the covariance matrix of the parameters, the posterior is approximately a bivariate normal distribution, $\phi(\omega, \theta) \propto \exp\left(-(1/2)(\omega - \mu_\omega, \theta - \mu_\theta)\boldsymbol{\Sigma}^{-1}(\omega - \mu_\omega, \theta - \mu_\theta)^{\intercal}\right)$, where $\boldsymbol{\Sigma} = [\sigma_\omega^2, \sigma_{\omega,\theta}; \sigma_{\omega,\theta}, \sigma_\theta^2]$ is the covariance matrix given in Eqs. (C.8)–(C.10). When considering a single parameter, ω or θ, one can calculate its posterior as $\phi(\omega) = \int_{-\infty}^{\infty}\phi(\omega, \theta)\mathrm{d}\theta \propto \exp\left(-(1/2)(\omega - \mu_\omega)^2/\sigma_\omega^2\right)$ and $\phi(\theta) = \int_{-\infty}^{\infty}\phi(\omega, \theta)\mathrm{d}\omega \propto \exp\left(-(1/2)(\theta - \mu_\theta)^2/\sigma_\theta^2\right)$ where $\phi(\omega)$ and $\phi(\theta)$ are the posterior probability distributions of ω and θ; these suggest that $\omega \sim \mathcal{N}(\mu_\omega, \sigma_\omega^2)$ and $\theta \sim \mathcal{N}(\mu_\theta, \sigma_\theta^2)$.

In this study, the problem of interest is somewhat different from the standard fitting problem because there is a prior constraint that the intercept must be positive. In this case, the prior probability is still constant when θ is positive but takes the value of zero when θ is negative. The posterior distribution of (ω, θ) becomes a truncated normal distribution, i.e., $\phi(\omega, \theta) \propto \exp\left(-(1/2)(\omega - \mu_\omega, \theta - \mu_\theta)\boldsymbol{\Sigma}^{-1}(\omega - \mu_\omega, \theta - \mu_\theta)^{\intercal}\right)$ if θ is positive and $\phi(\omega, \theta) = 0$ if θ is negative. The posterior probability distribution of θ is given by $\phi(\theta) = \int_{-\infty}^{\infty}\phi(\omega, \theta)\mathrm{d}\omega$, such that $\phi(\theta) \propto \exp\left(-(1/2)(\theta - \mu_\theta)^2/\sigma_\theta^2\right)$ if θ is positive and $\phi(\theta) = 0$ if θ is negative.

To assess the posterior distributions, we can also run Markov chain Monte Carlo (MCMC) simulations using the Metropolis–Hastings algorithm with the following steps:

(1) Choose an initial point, $(\omega, \theta) = (\omega_1, \theta_1)$.

(2) For the t-th step, propose a perturbed "candidate", $(\omega_t', \theta_t') = (\omega_t, \theta_t) + (\epsilon_{\omega,t}, \epsilon_{\theta,t})$.

(3) Calculate the acceptance ratio as $\lambda = \tilde{\mathcal{L}}(\omega_t', \theta_t')/\tilde{\mathcal{L}}(\omega_t, \theta_t)$, where $\tilde{\mathcal{L}}(\omega, \theta)$ is the "plug-in" likelihood (i.e., the maximum likelihood at given ω and θ values) given by Eq. (C.16). (Considering the "plug-in" likelihood with the "adjusted" X_i given by Eq. (C.16), instead of the "latent" x_i as an additional random variable in the simulation, may slightly underestimate the uncertainties of the parameters. However, this would guarantee the posterior to be maximized at the value given by the York regression, in which the "adjusted" X_i values are used.)

(4) Generate a uniformly distributed random number $r \in (0, 1)$, accept the perturbation and set $(\omega_{t+1}, \theta_{t+1}) = (\omega_t', \theta_t')$ if $\lambda > r$, or reject it and set $(\omega_{t+1}, \theta_{t+1}) = (\omega_t, \theta_t)$ if $\lambda \leqslant r$.

(5) Repeat steps (2)–(4) until t reaches a large enough number, and discard the samples from an initial "burn-in" period if necessary. If there is a priori constraint that the intercept must be positive, we should also discard all the samples with negative θ. Then, from the samples collected from the iteration, one can calculate the posterior distributions of the parameters.

The analyses in this section assume that the data errors are normally distributed. Strictly speaking, this assumption may be questionable, because the numbers of measurements contributing to the average concentration and matrix mass fraction for each carbonaceous chondrite group are limited. In principle, the errors should be described by student's t distributions, which would result in broader error distributions and larger uncertainties for the estimated parameters compared with those obtained under the normal distribution assumption. However, assuming t distributions would introduce additional complexity in modifying the widely applied methods of regression and error estimation, which is beyond the scope here. Moreover, the confidence intervals provided here, particularly those for the isotopic compositions, are already fairly broad from a practical perspective. For these reasons, we retain the assumption of normally distributed errors, despite the potential caveat discussed above.

Appendix D. Estimations of parameters and confidence intervals

Fitting the c and f data under the linear relation provided in the main text with the York method, we obtain the estimates of the parameters, μ_k and μ_b, together with their variance and covariance, σ_k^2, σ_b^2, and $\sigma_{k,b}$. From the discussion in Appendix C, we can write the posterior distribution function of the non-matrix concentration (the intercept b) as

$$\phi(c_{\rm NM}) = \begin{cases} (1/\Phi)\exp\left(-(1/2)\left(c_{\rm NM}-\mu_b\right)^2/\sigma_b^2\right) & \text{if} \quad c_{\rm NM} > 0, \\ 0 \quad \text{if} \quad c_{\rm NM} < 0, \end{cases} \tag{D.1}$$

where $\phi(c_{\rm NM})$ is the posterior probability distribution function of $c_{\rm NM} = b$ conditional on the data, and Φ is a normalizing factor given by $\Phi = \int_0^\infty \exp\left(-\left(b-\mu_b\right)^2/(2\sigma_b^2)\right) {\rm d}b$. When μ_b is large compared to σ_b, the distribution of Eq. (D.1) reduces to a normal distribution. In this case, μ_b gives the mode, expectation, and median of the distribution, and this value unambiguously gives the best estimate of parameter b. When μ_b is comparable to or smaller than σ_b (which could be the case for elements strongly depleted in the non-matrix component), the mode, expectation, and median of the distribution are no longer the same.

To further illustrate this effect, we show in Fig. D.8 (upper panel) the posterior distribution of $c_{\rm NM}$ calculated from the Eq. (D.1) together with that calculated from a MCMC simulation using the data of Zn. For the MCMC simulation, the initial choice of parameter is set as $(k_1, b_1) = (\mu_k, \mu_b)$, where μ_k and μ_b are the values suggested by the York fitting. The perturbations are set to follow $\epsilon_{k,t} \sim \mathcal{N}(0, \sigma_\epsilon^2)$ and $\epsilon_{b,t} \sim \mathcal{N}(0, \sigma_\epsilon^2)$, where σ_ϵ is set to 0.05 times the Zn concentration of the CI chondrite. The choice of the perturbations affects the efficiency of sampling but not the final distributions of the parameters as long as the number of iterations is sufficiently large. The number of iteration is set here to be 10^6. As we start with the maximum-likelihood estimation, we do not discard any initial samples. Since the intercept b must be positive, we discard samples with $b < 0$. As shown in Fig. D.8, the MCMC-generated posterior distribution is similar to the analytical expression of Eq. (D.1).

The relation between the non-matrix elemental concentration $c_{\rm NM}$ and non-matrix isotopic composition $\delta_{\rm NM}$ follows $\delta_{\rm NM} = \alpha/c_{\rm NM} + \beta$. Considering the uncertainty in $\delta_{\rm NM}$, we first focus on the contribution of $c_{\rm NM}$, which is the dominant source for elements like Zn and Te (Fig. 6). Assuming for now that $\alpha = \mu_\alpha$ and $\beta = \mu_\beta$ are exact, we have $\delta_{\rm NM} < \delta_{\rm NM}' < \delta_{\rm NM} + {\rm d}\delta_{\rm NM} \Leftrightarrow c_{\rm NM} < c_{\rm NM}' < c_{\rm NM} + {\rm d}c_{\rm NM}$, where $c_{\rm NM} = \mu_\alpha/(\delta_{\rm NM} - \mu_\beta)$ and ${\rm d}c_{\rm NM} = -\mu_\alpha/(\delta_{\rm NM} - \mu_\beta)^2 {\rm d}\delta_{\rm NM}$, such that $P(\delta_{\rm NM} < \delta_{\rm NM}' < \delta_{\rm NM} + {\rm d}\delta_{\rm NM}) = \varphi(\delta_{\rm NM}){\rm d}\delta_{\rm NM} = P(c_{\rm NM} < c_{\rm NM}' < c_{\rm NM} + {\rm d}c_{\rm NM}) = \phi(c_{\rm NM}){\rm d}c_{\rm NM}$, where $P(A)$ is the probability of event A and $\varphi(\delta_{\rm NM})$ is the probability distribution function of $\delta_{\rm NM}$. Hence, $\varphi(\delta_{\rm NM})$ is calculated as

$$\begin{aligned} \varphi(\delta_{\rm NM}) &= \phi(c_{\rm NM})({\rm d}c_{\rm NM}/{\rm d}\delta_{\rm NM}) \\ &= \phi(\mu_\alpha/(\delta_{\rm NM} - \mu_\beta))(-\mu_\alpha/(\delta_{\rm NM} - \mu_\beta)^2). \end{aligned} \tag{D.2}$$

An example calculated from the data of Zn is given in the right panel of Fig. D.8, where the results of Eq. (D.2) and the MCMC simulation are both provided and exhibit good agreement. (For the MCMC simulation, the samples in $\delta_{\rm NM}$ are calculated from those in $c_{\rm NM}$ following $\delta_{\rm NM} = \alpha/c_{\rm NM} + \beta$.) Due to the nonlinear transformation, the mode of the distribution $\phi(c_{\rm NM})$ does not occur at $\mu_\alpha/\mu_b + \mu_\beta$. Calculating the derivative ${\rm d}\varphi/{\rm d}\delta_{\rm NM}$, one can find that the mode of the distribution $\varphi(\delta_{\rm NM})$ occurs at $\mu_\alpha/\left(\mu_b/2 + \sqrt{(\mu_b/2)^2 + 2\sigma_b^2}\right) + \mu_\beta$, whose value is larger than $\mu_\alpha/\mu_b + \mu_\beta$ given that μ_α is negative. The discrepancy between the two modes is clear from the example shown in Fig. D.8, in which the $(c_{\rm NM}, \delta_{\rm NM})$ point defined by the modes of $\phi(c_{\rm NM})$ and $\varphi(\delta_{\rm NM})$ do not fall on curve $\delta_{\rm NM} = \mu_\alpha/c_{\rm NM} + \mu_\beta$. This discrepancy is particularly significant when $\mu_b \lesssim \sigma_b$. With this concern, in addition to the modes, we also consider the medians of the two distributions, $c_{\rm NM}^{\rm m}$ and $\delta_{\rm NM}^{\rm m}$, which are obtained from

$$P(c_{\rm NM} < c_{\rm NM}^{\rm m}) = \int_0^{c_{\rm NM}^{\rm m}} \phi(c_{\rm NM}){\rm d}c_{\rm NM} = 0.5, \tag{D.3}$$

$$P(\delta_{\rm NM} < \delta_{\rm NM}^{\rm m}) = \int_{-\infty}^{\delta_{\rm NM}^{\rm m}} \varphi(\delta_{\rm NM}){\rm d}\delta_{\rm NM} = 0.5. \tag{D.4}$$

The relation between $c_{\rm NM}$ and $\delta_{\rm NM}$ is monotonic; thus, $c_{\rm NM} < c_{\rm NM}^{\rm m} \Leftrightarrow \delta_{\rm NM} < \mu_\alpha/c_{\rm NM}^{\rm m} + \mu_\beta$. This guarantees the consistency between the two medians, i.e., $\delta_{\rm NM}^{\rm m} = \mu_\alpha/c_{\rm NM}^{\rm m} + \mu_\beta$. This is also illustrated in Fig. D.8, where $(c_{\rm NM}^{\rm m}, \delta_{\rm NM}^{\rm m})$ falls exactly on the curve $\delta_{\rm NM} = \mu_\alpha/c_{\rm NM} + \mu_\beta$.

If the c-f fitting leads to $\mu_b \gg \sigma_b$, the mode and median of $\phi(c_{\rm NM})$ are both μ_b. If the fitting leads to $\mu_b \lesssim \sigma_b$, the mode and median of $\phi(c_{\rm NM})$ are different, but their difference is not significant. From the property of the normal distribution function, one can show that the difference is less than $\sim 0.7\sigma_b$ as long as μ_b is positive. Either way, the c-f fitting does not distinguish between the mode and median values; meanwhile, the consistency between $c_{\rm NM}$ and $\delta_{\rm NM}$ is guaranteed when we choose the medians of both quantities as the best estimates. For these reasons, we choose the medians, $c_{\rm NM}^{\rm m}$ and $\delta_{\rm NM}^{\rm m}$, as the best estimates for the elemental concentration and isotopic composition of the non-matrix component.

Now we consider the confidence intervals of $c_{\rm NM}$ and $\delta_{\rm NM}$. From Eq. (D.1), we estimate the 95% confidence interval of $c_{\rm NM}$, denoted by $(c_{\rm NM}^{\rm ll}, c_{\rm NM}^{\rm ul})$, through

$$\int_0^{c_{\rm NM}^{\rm ll}} \phi(c_{\rm NM}){\rm d}c_{\rm NM} = \int_{c_{\rm NM}^{\rm ul}}^{\infty} \phi(c_{\rm NM}){\rm d}c_{\rm NM} = 0.025. \tag{D.5}$$

Here, superscripts "ll" and "ul" represent lower limit and upper limit, respectively. From the confidence interval of $c_{\rm NM}$, we can further assess

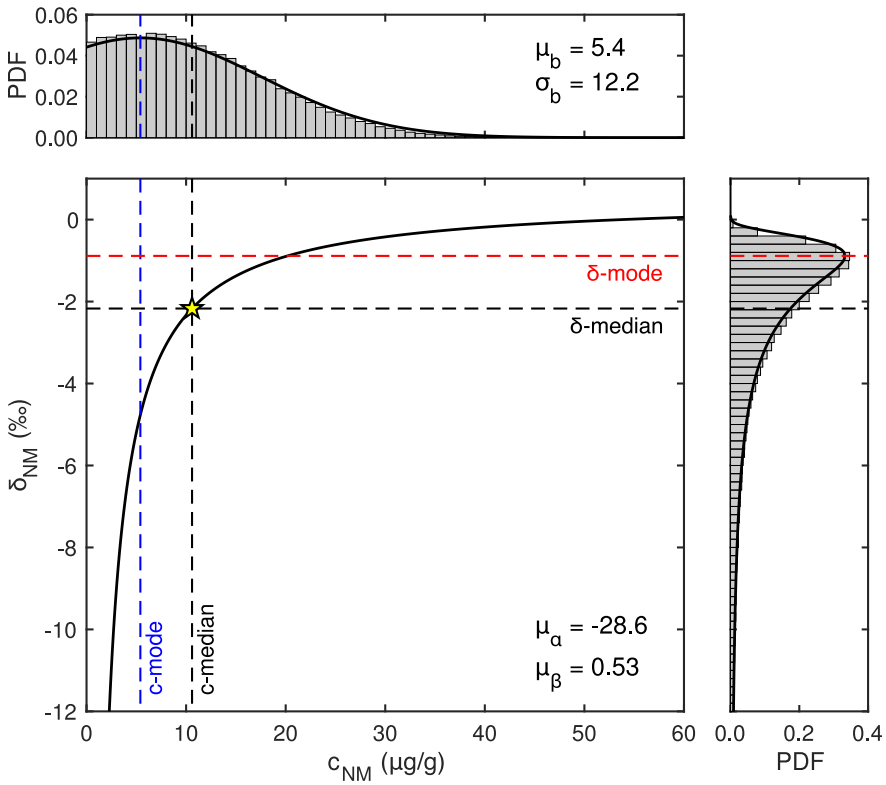

Fig. D.8. An example for the relation between the concentration (c_{NM}) and isotopic composition (δ_{NM}) of the non-matrix component. The main panel shows their relation constrained by isotopic measurements of chondrite samples, $\delta_{NM} = \mu_\alpha/c_{NM} + \mu_\beta$. The upper panel shows the posterior probability distribution function (PDF) of c_{NM} from the c-f fitting. The black curve gives the analytical PDF of Eq. (D.1), and the histogram gives the results from a Markov chain Monte Carlo (MCMC) simulation (see Appendix D for details). The dashed blue and black lines give the mode and median of the analytical distribution. The right panel gives the PDF of δ_{NM}. The black curve gives the analytical result of Eq. (D.2), and the histogram gives the MCMC simulation results. The dashed red and black lines give the mode and median of the analytical distribution. The values of μ_b, σ_b, μ_α, and μ_β are given in the figure and are from the fitting for Zn.

that of δ_{NM}. So far, we have treated the estimates of α and β as exact. Under this assumption, the 95% confidence interval of δ_{NM}, $(\delta^{ll}_{NM}, \delta^{ul}_{NM})$, is determined solely by that of c_{NM}, such that $\delta^{ll}_{NM} = \mu_\alpha/c^{ll}_{NM} + \mu_\beta$ and $\delta^{ul}_{NM} = \mu_\alpha/c^{ul}_{NM} + \mu_\beta$. Then, we also account for the uncertainties in α and β, which are characterized by their variance and covariance obtained from the York fitting, σ^2_α, σ^2_β, and $\sigma_{\alpha,\beta}$. Focusing on the uncertainties in α and β, the 95% confidence interval of $\delta^m_{NM} = \alpha/c^m_{NM} + \beta$ is expressed as $(\mu_\alpha/c^m_{NM} + \mu_\beta - 2\zeta^m_\delta, \mu_\alpha/c^m_{NM} + \mu_\beta + 2\zeta^m_\delta)$, where ζ^m_δ is the standard error of prediction at $c_{NM} = c^m_{NM}$ given by

$$\zeta^m_\delta = \sqrt{(1/c^m_{NM})^2\sigma^2_\alpha + \sigma^2_\beta + (2/c^m_{NM})\sigma_{\alpha,\beta}}. \quad (D.6)$$

As discussed in Appendix D, we ignore the potential effects of t distributions and assume normal distributions for the errors, such that the 95% confidence interval corresponds to the range of $\mu_\alpha/c^m_{NM} + \mu_\beta \pm 2\zeta^m_\delta$. Including contributions of c_{NM}, α, and β, we estimate δ^{ll}_{NM} and δ^{ul}_{NM} as

$$\left(\delta^{ll}_{NM} - \delta^m_{NM}\right)^2 = \left[\mu_\alpha(1/c^{ll}_{NM} - 1/c^m_{NM})\right]^2 + (2\zeta^m_\delta)^2, \quad (D.7)$$

$$\left(\delta^{ul}_{NM} - \delta^m_{NM}\right)^2 = \left[\mu_\alpha(1/c^{ul}_{NM} - 1/c^m_{NM})\right]^2 + (2\zeta^m_\delta)^2. \quad (D.8)$$

Applying the δ-$1/c$ relation and the c_{NM} value, we estimate the mass-dependent isotopic fractionation between the CI-like matrix and isotopically light non-matrix component as

$$\Delta^m_{NM} = \delta^m_M - \delta^m_{NM} = \mu_\alpha(1/c^m_M - 1/c^m_{NM}), \quad (D.9)$$

where c^m_M is the concentration in matrix component and is taken as that of the average CI chondrite value, as listed in Table 1. The second equality assumes that $\delta^m_M = \mu_\alpha/c^m_M + \mu_\beta$, i.e., the isotopic composition of the matrix component is calculated from the fitted δ–$1/c$ relation together with the CI chondrite concentration. As shown in Fig. 6, except for Ga, the calculated δ^m_M matches very well with the measured isotopic compositions of CI chondrites. We also estimate the 95% confidence interval of Δ_{NM}, $(\Delta^{ll}_{NM}, \Delta^{ul}_{NM})$, following

$$\left(\Delta^{ll}_{NM} - \Delta^m_{NM}\right)^2 = \left[\mu_\alpha(1/c^{ul}_{NM} - 1/c^m_{NM})\right]^2 + 4\left(1/c_M - 1/c^m_{NM}\right)^2\sigma^2_\alpha, \quad (D.10)$$

$$\left(\Delta^{ul}_{NM} - \Delta^m_{NM}\right)^2 = \left[\mu_\alpha(1/c^{ll}_{NM} - 1/c^m_{NM})\right]^2 + 4\left(1/c_M - 1/c^m_{NM}\right)^2\sigma^2_\alpha, \quad (D.11)$$

Here, we have neglected the uncertainty in $1/c_M$ because it is typically small compared to that in $1/c_{NM}$. For Zn, Te, and Cd, because of the very low values of c^{ll}_{NM}, the confidence intervals of Δ_{NM} extend to unrealistically high values. For these elements, we consider the upper limit in the mass-dependent fractionation as the theoretical value of the kinetic condensation limit, $\Delta^{ul}_{NM} = 1000‰ \times |\sqrt{M_j/M_i} - 1|$, where M_i and M_j are the molar masses of the heavy and light isotopes, respectively (e.g., Richter, 2004). For the confidence intervals of δ_{NM}, we also discard the values that lead to fractionations greater than the kinetic condensation limit.

Appendix E. Supplementary data

Supplementary material related to this article can be found online at https://doi.org/10.1016/j.icarus.2026.117049.

Data availability

All data needed to evaluate the conclusions in the paper are present in the paper and/or the Supplementary Material.

References

Alexander, C., 2005. Re-examining the role of chondrules in producing the elemental fractionations in chondrites. Meteorit. Planet. Sci. 40 (7), 943–965. http://dx.doi.org/10.1111/j.1945-5100.2005.tb00166.x.

Alexander, C., 2019. Quantitative models for the elemental and isotopic fractionations in chondrites: The carbonaceous chondrites. Geochim. Cosmochim. Acta 254, 277–309. http://dx.doi.org/10.1016/j.gca.2019.02.008.

Alexander, C., Ebel, D.S., 2012. Questions, questions: Can the contradictions between the petrologic, isotopic, thermodynamic, and astrophysical constraints on chondrule formation be resolved? Meteorit. Planet. Sci. 47 (7), 1157–1175. http://dx.doi.org/10.1111/j.1945-5100.2011.01308.x.

Alexander, C., Wynn, J.G., Bowden, R., 2022. Sulfur abundances and isotopic compositions in bulk carbonaceous chondrites and insoluble organic material: Clues to elemental and isotopic fractionations of volatile chalcophiles. Meteorit. Planet. Sci. 57 (2), 334–351. http://dx.doi.org/10.1111/maps.13746.

Anders, E., 1964. Origin, age, and composition of meteorites. Space Sci. Rev. 3 (5), 583–714. http://dx.doi.org/10.1007/BF00177954.

Baker, R., Schönbächler, M., Rehkämper, M., Williams, H., Halliday, A., 2010. The thallium isotope composition of carbonaceous chondrites—New evidence for live ^{205}Pb in the early solar system. Earth Planet. Sci. Lett. 291 (1–4), 39–47. http://dx.doi.org/10.1016/j.epsl.2009.12.044.

Blinova, A.I., Zega, T.J., Herd, C.D., Stroud, R.M., 2014. Testing variations within the Tagish Lake meteorite—I: Mineralogy and petrology of pristine samples. Meteorit. Planet. Sci. 49 (4), 473–502. http://dx.doi.org/10.1111/maps.12271.

Braukmüller, N., Funk, C., Abouchami, W., Pickard, H., Rehkämper, M., Bragagni, A., Galer, S.J., Münker, C., Becker, H., Wombacher, F., 2025. Moderately volatile elements in chondrites record chondrule formation, two-component mixing and redistribution on parent bodies. Geochim. Cosmochim. Acta 393, 43–62. http://dx.doi.org/10.1016/j.gca.2025.02.001.

Braukmüller, N., Wombacher, F., Funk, C., Münker, C., 2019. Earth's volatile element depletion pattern inherited from a carbonaceous chondrite-like source. Nat. Geosci. 12 (7), 564–568. http://dx.doi.org/10.1038/s41561-019-0375-x.

Braukmüller, N., Wombacher, F., Hezel, D.C., Escoube, R., Münker, C., 2018. The chemical composition of carbonaceous chondrites: Implications for volatile element depletion, complementarity and alteration. Geochim. Cosmochim. Acta 239, 17–48. http://dx.doi.org/10.1016/j.gca.2018.07.023.

Brearley, A.J., Krot, A.N., 2013. Metasomatism in the early solar system: The record from chondritic meteorites. In: Metasomatism and the Chemical Transformation of Rock: The Role of Fluids in Terrestrial and Extraterrestrial Processes. Springer, pp. 659–789. http://dx.doi.org/10.1007/978-3-642-28394-9_15.

Bryson, J.F., Brennecka, G.A., 2021. Constraints on chondrule generation, disk dynamics, and asteroid accretion from the compositions of carbonaceous meteorites. Astrophys. J. 912 (2), 163. http://dx.doi.org/10.3847/1538-4357/abea12.

Connolly, H.C., Jones, R.H., 2016. Chondrules: The canonical and noncanonical views. J. Geophys. Res.: Planets 121 (10), 1885–1899. http://dx.doi.org/10.1002/2016JE005113.

Davis, A.M., 2006. Volatile evolution and loss. Meteorites the Early Sol. Syst. II 1, 295–307.

Desch, S.J., Morris, M.A., Connolly, Jr., H.C., Boss, A.P., 2012. The importance of experiments: Constraints on chondrule formation models. Meteorit. Planet. Sci. 47 (7), 1139–1156. http://dx.doi.org/10.1111/j.1945-5100.2012.01357.x.

Gattacceca, J., Bonal, L., Sonzogni, C., Longerey, J., 2020. CV chondrites: More than one parent body. Earth Planet. Sci. Lett. 547, 116467. http://dx.doi.org/10.1016/j.epsl.2020.116467.

Gattacceca, J., Gounelle, M., Devouard, B., Barrat, J.A., Bonal, L., King, A., Maurel, C., Beck, P., Roskosz, M., Viennet, J.-C., et al., 2025. Oued Chebeika 002: A new CI1 meteorite linked to outer solar system bodies. Meteorit. Planet. Sci. http://dx.doi.org/10.1111/maps.14359.

Grossman, J.N., Brearley, A.J., 2005. The onset of metamorphism in ordinary and carbonaceous chondrites. Meteorit. Planet. Sci. 40 (1), 87–122. http://dx.doi.org/10.1111/j.1945-5100.2005.tb00366.x.

Hellmann, J.L., Hopp, T., Burkhardt, C., Kleine, T., 2020. Origin of volatile element depletion among carbonaceous chondrites. Earth Planet. Sci. Lett. 549, 116508. http://dx.doi.org/10.1016/j.epsl.2020.116508.

Hellmann, J.L., Schneider, J.M., Wölfer, E., Drażkowska, J., Jansen, C.A., Hopp, T., Burkhardt, C., Kleine, T., 2023. Origin of isotopic diversity among carbonaceous chondrites. Astrophys. J. Lett. 946 (2), L34. http://dx.doi.org/10.3847/2041-8213/acc102.

Hewins, R.H., Bourot-Denise, M., Zanda, B., Leroux, H., Barrat, J.-A., Humayun, M., Göpel, C., Greenwood, R.C., Franchi, I.A., Pont, S., et al., 2014. The Paris meteorite, the least altered CM chondrite so far. Geochim. Cosmochim. Acta 124, 190–222. http://dx.doi.org/10.1016/j.gca.2013.09.014.

Howard, K., Alexander, C.O., Schrader, D., Dyl, K., 2015. Classification of hydrous meteorites (CR, CM and C2 ungrouped) by phyllosilicate fraction: PSD-XRD modal mineralogy and planetesimal environments. Geochim. Cosmochim. Acta 149, 206–222. http://dx.doi.org/10.1016/j.gca.2014.10.025.

Hu, Y., Moynier, F., Dai, W., Paquet, M., Yokoyama, T., Abe, Y., Aléon, J., Alexander, C.M., Amari, S., Amelin, Y., et al., 2024. Pervasive aqueous alteration in the early solar system revealed by potassium isotopic variations in Ryugu samples and carbonaceous chondrites. Icarus 409, 115884. http://dx.doi.org/10.1016/j.icarus.2023.115884.

Humayun, M., 2012. Chondrule cooling rates inferred from diffusive profiles in metal lumps from the acfer 097 CR2 chondrite. Meteorit. Planet. Sci. 47 (7), 1191–1208. http://dx.doi.org/10.1111/j.1945-5100.2012.01371.x.

Jacquet, E., Marrocchi, Y., Charnoz, S., 2026. Alkali recondensation into chondrules. Icarus 116970. http://dx.doi.org/10.1016/j.icarus.2026.116970.

Jenkins, L.E., Lee, M.R., Daly, L., King, A.J., Floyd, C.J., Martin, P.E., Almeida, N.V., Genge, M.J., 2024. Winchcombe: An example of rapid terrestrial alteration of a CM chondrite. Meteorit. Planet. Sci. 59 (5), 988–1005. http://dx.doi.org/10.1111/maps.13949.

Jiang, Y., Koefoed, P., Pravdivtseva, O., Chen, H., Li, C.H., Huang, F., Qin, L.P., Liu, J., Wang, K., 2021. Early solar system aqueous activity: K isotope evidence from Allende. Meteorit. Planet. Sci. 56 (1), 61–76. http://dx.doi.org/10.1111/maps.13588.

Jones, R.H., 2012. Petrographic constraints on the diversity of chondrule reservoirs in the protoplanetary disk. Meteorit. Planet. Sci. 47 (7), 1176–1190. http://dx.doi.org/10.1111/j.1945-5100.2011.01327.x.

Kallemeyn, G.W., Wasson, J.T., 1982. The compositional classification of chondrites: III. Ungrouped carbonaceous chondrites. Geochim. Cosmochim. Acta 46 (11), 2217–2228. http://dx.doi.org/10.1111/j.1945-5100.2011.01327.x.

Kato, C., Moynier, F., 2017. Gallium isotopic evidence for the fate of moderately volatile elements in planetary bodies and refractory inclusions. Earth Planet. Sci. Lett. 479, 330–339. http://dx.doi.org/10.1016/j.epsl.2017.09.028.

Kita, N.T., Nagahara, H., Tachibana, S., Tomomura, S., Spicuzza, M.J., Fournelle, J.H., Valley, J.W., 2010. High precision SIMS oxygen three isotope study of chondrules in LL3 chondrites: Role of ambient gas during chondrule formation. Geochim. Cosmochim. Acta 74 (22), 6610–6635. http://dx.doi.org/10.1016/j.gca.2010.08.011.

Kong, P., Ebihara, M., Palme, H., 1999. Distribution of siderophile elements in CR chondrites: Evidence for evaporation and recondensation during chondrule formation. Geochim. Cosmochim. Acta 63 (17), 2637–2652. http://dx.doi.org/10.1016/S0016-7037(99)00157-X.

Kong, P., Palme, H., 1999. Compositional and genetic relationship between chondrules, chondrule rims, metal, and matrix in the Renazzo chondrite. Geochim. Cosmochim. Acta 63 (21), 3673–3682. http://dx.doi.org/10.1016/S0016-7037(99)00110-6.

van Kooten, E.M., Brearley, A., Ebel, D.S., Alexander, C.M., Gemma, M.E., Hezel, D.C., 2024. Is there a genetic relationship between chondrules and matrix? Space Sci. Rev. 220 (7), 74. http://dx.doi.org/10.1007/s11214-024-01107-9.

van Kooten, E., Moynier, F., 2019. Zinc isotope analyses of singularly small samples (< 5 ng Zn): Investigating chondrule-matrix complementarity in Leoville. Geochim. Cosmochim. Acta 261, 248–268. http://dx.doi.org/10.1016/j.gca.2019.07.022.

van Kooten, E., Schiller, M., Moynier, F., Johansen, A., Haugbølle, T., Bizzarro, M., 2021. Hybrid accretion of carbonaceous chondrites by radial transport across the Jupiter barrier. Astrophys. J. 910 (1), 70. http://dx.doi.org/10.3847/1538-4357/abd9c8.

Larimer, J.W., Anders, E., 1967. Chemical fractionations in meteorites—II. Abundance patterns and their interpretation. Geochim. Cosmochim. Acta 31 (8), 1239–1270. http://dx.doi.org/10.1016/S0016-7037(67)80014-0.

Lauretta, D.S., Connolly, Jr., H.C., Aebersold, J.E., Alexander, C.M.O., Ballouz, R.-L., Barnes, J.J., Bates, H.C., Bennett, C.A., Blanche, L., Blumenfeld, E.H., et al., 2024. Asteroid (101955) Bennu in the laboratory: Properties of the sample collected by OSIRIS-REx. Meteorit. Planet. Sci. 59 (9), 2453–2486. http://dx.doi.org/10.1111/maps.14227.

Lodders, K., Fegley, B., Mezger, K., Ebel, D., 2025. Condensation and the volatility trend of the Earth. Space Sci. Rev. 221 (5), 54. http://dx.doi.org/10.1007/s11214-025-01182-6.

Luais, B., Florin, G., 2025. Origin of the mass-dependent germanium isotopic continuum in the early solar system. Earth Planet. Sci. Lett. 672, 119663. http://dx.doi.org/10.1016/j.epsl.2025.119663.

Luck, J.M., Othman, D.B., Albarède, F., 2005. Zn and Cu isotopic variations in chondrites and iron meteorites: Early solar nebula reservoirs and parent-body processes. Geochim. Cosmochim. Acta 69 (22), 5351–5363. http://dx.doi.org/10.1016/j.gca.2005.06.018.

Luck, J., Othman, D.B., Barrat, J., Albarède, F., 2003. Coupled ^{63}Cu and ^{16}O excesses in chondrites. Geochim. Cosmochim. Acta 67 (1), 143–151. http://dx.doi.org/10.1016/S0016-7037(02)01038-4.

Macke, R.J., Consolmagno, G.J., Britt, D.T., 2011. Density, porosity, and magnetic susceptibility of carbonaceous chondrites. Meteorit. Planet. Sci. 46 (12), 1842–1862. http://dx.doi.org/10.1111/j.1945-5100.2011.01298.x.

Marrocchi, Y., Jones, R.H., Russell, S.S., Hezel, D.C., Barosch, J., Kuznetsova, A., 2024. Chondrule properties and formation conditions. Space Sci. Rev. 220 (6), 69. http://dx.doi.org/10.1007/s11214-024-01102-0.

Morton, E.M., Pickard, H., Wombacher, F., Huang, Y., Palk, E., Martins, R., Kuthning, S., Schönbächler, M., Rehkämper, M., 2024. Volatile element depletion of carbonaceous chondrites—Insights from mass-dependent zinc, cadmium, and tellurium isotope variations. Astrophys. J. 977 (1), 53. http://dx.doi.org/10.3847/1538-4357/ad87ed.

Nie, N.X., Chen, X.Y., Hopp, T., Hu, J.Y., Zhang, Z.J., Teng, F.Z., Shahar, A., Dauphas, N., 2021. Imprint of chondrule formation on the K and Rb isotopic compositions of carbonaceous meteorites. Sci. Adv. 7 (49), eabl3929. http://dx.doi.org/10.1126/sciadv.abl3929.

Palme, H., Lodders, K., Jones, A., 2014. 2.2-Solar System abundances of the elements. In: Holland, H.D., Turekian, K.K. (Eds.), Treatise on Geochemistry (Second Edition), second ed. Elsevier, Oxford, pp. 15–36. http://dx.doi.org/10.1016/B978-0-08-095975-7.00118-2.

Paquet, M., Moynier, F., Yokoyama, T., Dai, W., Hu, Y., Abe, Y., Aléon, J., O'D. Alexander, C.M., Amari, S., Amelin, Y., et al., 2023. Contribution of Ryugu-like material to Earth's volatile inventory by Cu and Zn isotopic analysis. Nat. Astron. 7 (2), 182–189. http://dx.doi.org/10.1038/s41550-022-01846-1.

Patzer, A., Bullock, E.S., Alexander, C., 2021. Testing models for the compositions of chondrites and their components: I. CO chondrites. Geochim. Cosmochim. Acta 304, 119–140. http://dx.doi.org/10.1016/j.gca.2021.04.004.

Patzer, A., Bullock, E.S., Alexander, C., 2022. Testing models for the compositions of chondrites and their components: II. CR chondrites. Geochim. Cosmochim. Acta 319, 1–29. http://dx.doi.org/10.1016/j.gca.2021.12.021.

Patzer, A., Bullock, E.S., Alexander, C., 2023. Testing models for the compositions of chondrites and their components: III. CM chondrites. Geochim. Cosmochim. Acta 359, 30–45. http://dx.doi.org/10.1016/j.gca.2023.08.021.

Pringle, E.A., Moynier, F., Beck, P., Paniello, R., Hezel, D.C., 2017. The origin of volatile element depletion in early solar system material: Clues from Zn isotopes in chondrules. Earth Planet. Sci. Lett. 468, 62–71. http://dx.doi.org/10.1016/j.epsl.2017.04.002.

Richter, F.M., 2004. Timescales determining the degree of kinetic isotope fractionation by evaporation and condensation. Geochim. Cosmochim. Acta 68 (23), 4971–4992. http://dx.doi.org/10.1016/j.gca.2004.06.008.

Richter, F.M., Dauphas, N., Teng, F.Z., 2009. Non-traditional fractionation of non-traditional isotopes: evaporation, chemical diffusion and soret diffusion. Chem. Geol. 258 (1–2), 92–103. http://dx.doi.org/10.1016/j.chemgeo.2008.06.011.

Richter, F.M., Liang, Y., Davis, A.M., 1999. Isotope fractionation by diffusion in molten oxides. Geochim. Cosmochim. Acta 63 (18), 2853–2861. http://dx.doi.org/10.1016/S0016-7037(99)00164-7.

Schrader, D.L., Franchi, I.A., Connolly Jr., H.C., Greenwood, R.C., Lauretta, D.S., Gibson, J.M., 2011. The formation and alteration of the Renazzo-like carbonaceous chondrites I: Implications of bulk-oxygen isotopic composition. Geochim. Cosmochim. Acta 75 (1), 308–325. http://dx.doi.org/10.1016/j.gca.2010.09.028.

Singerling, S.A., Sutton, S.R., Lanzirotti, A., Newville, M., Brearley, A.J., 2021. Trace elemental behavior in the solar nebula: Synchrotron X-ray fluorescence analyses of CM and CR chondritic iron sulfides and associated metal. Geochim. Cosmochim. Acta 310, 131–154. http://dx.doi.org/10.1016/j.gca.2021.07.016.

Sossi, P.A., Klemme, S., O'Neill, H.S.C., Berndt, J., Moynier, F., 2019. Evaporation of moderately volatile elements from silicate melts: Experiments and theory. Geochim. Cosmochim. Acta 260, 204–231. http://dx.doi.org/10.1016/j.gca.2019.06.021.

Stewart, S.T., Lock, S.J., Carter, P.J., Davies, E.J., Petaev, M.I., Jacobsen, S.B., 2025. Planetesimal impact vapor plumes and nebular shocks form chondritic mixtures. Planet. Sci. J. 6 (5), 108. http://dx.doi.org/10.3847/PSJ/adbe71.

Titterington, D.M., Halliday, A.N., 1979. On the fitting of parallel isochrons and the method of maximum likelihood. Chem. Geol. 26 (3–4), 183–195. http://dx.doi.org/10.1016/0009-2541(79)90045-7.

Wasson, J.T., Isa, J., Rubin, A.E., 2013. Compositional and petrographic similarities of CV and CK chondrites: A single group with variations in textures and volatile concentrations attributable to impact heating, crushing and oxidation. Geochim. Cosmochim. Acta 108, 45–62. http://dx.doi.org/10.1016/j.gca.2013.01.011.

Watkins, J.M., DePaolo, D.J., Watson, E.B., 2017. Kinetic fractionation of non-traditional stable isotopes by diffusion and crystal growth reactions. Rev. Miner. Geochem. 82 (1), 85–125. http://dx.doi.org/10.2138/rmg.2017.82.4.

Wölfer, E., Burkhardt, C., Nimmo, F., Kleine, T., 2025. Origin of moderately volatile elements in Earth inferred from mass-dependent Ge isotope variations among chondrites. Earth Planet. Sci. Lett. 663, 119435. http://dx.doi.org/10.1016/j.epsl.2025.119435.

Wood, B.J., Smythe, D.J., Harrison, T., 2019. The condensation temperatures of the elements: A reappraisal. Am. Mineral. 104 (6), 844–856. http://dx.doi.org/10.2138/am-2019-6852CCBY.

Yokoyama, T., Nagashima, K., Nakai, I., Young, E.D., Abe, Y., Aléon, J., Alexander, C.M.O., Amari, S., Amelin, Y., ichi Bajo, K., Bizzarro, M., Bouvier, A., Carlson, R.W., Chaussidon, M., Choi, B.-G., Dauphas, N., Davis, A.M., Rocco, T.D., Fujiya, W., Fukai, R., Gautam, I., Haba, M.K., Hibiya, Y., Hidaka, H., Homma, H., Hoppe, P., Huss, G.R., Ichida, K., Iizuka, T., Ireland, T.R., Ishikawa, A., Ito, M., Itoh, S., Kawasaki, N., Kita, N.T., Kitajima, K., Kleine, T., Komatani, S., Krot, A.N., Liu, M.-C., Masuda, Y., McKeegan, K.D., Morita, M., Motomura, K., Moynier, F., Nguyen, A., Nittler, L., Onose, M., Pack, A., Park, C., Piani, L., Qin, L., Russell, S.S., Sakamoto, N., Schönbächler, M., Tafla, L., Tang, H., Terada, K., Terada, Y., Usui, T., Wada, S., Wadhwa, M., Walker, R.J., Yamashita, K., Yin, Q.-Z., Yoneda, S., Yui, H., Zhang, A.-C., Connolly, H.C., Lauretta, D.S., Nakamura, T., Naraoka, H., Noguchi, T., Okazaki, R., Sakamoto, K., Yabuta, H., Abe, M., Arakawa, M., Fujii, A., Hayakawa, M., Hirata, N., Hirata, N., Honda, R., Honda, C., Hosoda, S., ichi Iijima, Y., Ikeda, H., Ishiguro, M., Ishihara, Y., Iwata, T., Kawahara, K., Kikuchi, S., Kitazato, K., Matsumoto, K., Matsuoka, M., Michikami, T., Mimasu, Y., Miura, A., Morota, T., Nakazawa, S., Namiki, N., Noda, H., Noguchi, R., Ogawa, N., Ogawa, K., Okada, T., Okamoto, C., Ono, G., Ozaki, M., Saiki, T., Sakatani, N., Sawada, H., Senshu, H., Shimaki, Y., Shirai, K., Sugita, S., Takei, Y., Takeuchi, H., Tanaka, S., Tatsumi, E., Terui, F., Tsuda, Y., Tsukizaki, R., Wada, K., ichiro Watanabe, S., Yamada, M., Yamada, T., Yamamoto, Y., Yano, H., Yokota, Y., Yoshihara, K., Yoshikawa, M., Yoshikawa, K., Furuya, S., Hatakeda, K., Hayashi, T., Hitomi, Y., Kumagai, K., Miyazaki, A., Nakato, A., Nishimura, M., Soejima, H., Suzuki, A., Yada, T., Yamamoto, D., Yogata, K., Yoshitake, M., Tachibana, S., Yurimoto, H., 2023. Samples returned from the asteroid Ryugu are similar to Ivuna-type carbonaceous meteorites. Science 379 (6634), eabn7850. http://dx.doi.org/10.1126/science.abn7850.

York, D., Evensen, N.M., Martınez, M.L., De Basabe Delgado, J., 2004. Unified equations for the slope, intercept, and standard errors of the best straight line. Am. J. Phys. 72 (3), 367–375. http://dx.doi.org/10.1119/1.1632486.

Zhang, Y., Ni, H., Chen, Y., 2010. Diffusion data in silicate melts. Rev. Miner. Geochem. 72 (1), 311–408. http://dx.doi.org/10.2138/rmg.2010.72.8.

Zhang, Z.J., Nie, N.X., Mendybaev, R.A., Liu, M.C., Hu, J.J., Hopp, T., Alp, E.E., Lavina, B., Bullock, E.S., McKeegan, K.D., et al., 2021. Loss and isotopic fractionation of alkali elements during diffusion-limited evaporation from molten silicate: Theory and experiments. ACS Earth Space Chem. 5 (4), 755–784. http://dx.doi.org/10.1021/acsearthspacechem.0c00263.